ACCSCIENCE PUBLISHING

International Journal of Bioprinting

RESEARCH ARTICLE

Three-dimensional-printed hydroxyapatite/nanoclay/polycaprolactone composite scaffold for immunomodulation and bone defect repair

Xiang Li[1,2†], Zhenyu Wen[1†], Jiaxiang Song[1], Hao Tang[1], Wanshun Liu[1], Xitao Linghu[1], Shuai Huang[3*], Weikang Xu[2,4*], and Qingde Wa[1*]

[1]Department of Orthopedic Surgery, The Second Affiliated Hospital of Zunyi Medical University, Zunyi, Guizhou, China

[2]Medical Materials and Engineering Research Laboratory, Institute of Biological and Medical Engineering, Guangdong Academy of Sciences, Guangzhou, Guangdong, China

[3]Department of Orthopedic Surgery, The First People's Hospital of Foshan, Foshan, Guangdong, China

[4]Guangdong Provincial Key Laboratory of Medical Electronic Instruments and Materials, Guangdong Institute of Medical Instruments, National Engineering Research Center for Healthcare Devices, Guangzhou, Guangdong, China

[†]These authors contributed equally to this work.

***Corresponding authors:**
Shuai Huang
(huangshuai85315@163.com)

Weikang Xu
(759200816@qq.com)

Qingde Wa
(wqd887zsy@126.com)

Citation: Li X, Wen Z, Song J, *et al.* Three-dimensional-printed hydroxyapatite/nanoclay/polycaprolactone composite scaffold for immunomodulation and bone defect repair. *Int J Bioprint.* 2025;11(3):434-456. doi: 10.36922/IJB025170162

Received: February 20, 2025
Revised: April 24, 2025
Accepted: May 13, 2025
Published online: May 16, 2025

Abstract

Excessive inflammation remains a major impediment to the clinical repair of critical-sized bone defects, with the immune micro-environment playing a pivotal role in osteogenesis. An appropriate local immune response following biomaterial implantation is essential for successful bone tissue regeneration. In this study, a hydroxyapatite/montmorillonite nanoclay/polycaprolactone (HNP) composite scaffold was designed and subsequently fabricated using three-dimensional (3D) printing, with the aim of modulating macrophage polarization and promoting bone regeneration. The resulting HNP scaffold exhibited favorable mechanical strength and significantly promoted bone marrow mesenchymal stem cell adhesion, proliferation, secretion of osteogenic cytokines, and osteogenic differentiation. Moreover, it modulated the bone immune micro-environment by suppressing M1 macrophage polarization and promoting a shift toward the M2 phenotype, thereby establishing a pro-osteogenic immune milieu. *In vivo* studies using a rat calvarial defect model demonstrated that, compared with other groups, the HNP scaffold markedly enhanced M2 macrophage polarization, promoted angiogenesis, and accelerated new bone formation. Overall, the 3D-printed HNP scaffold effectively regulated the immune micro-environment and facilitated both bone regeneration and neovascularization, highlighting its strong potential as a candidate for bone tissue engineering applications.

***Keywords*:** Bone repair; Hydroxyapatite; Macrophage polarization; Nanoclay; Three-dimensional printing

1. Introduction

Bone defects arise from disruptions in skeletal integrity caused by factors such as congenital deformities, trauma, disease, or surgical excision, resulting in localized or widespread bone loss. These defects often lead to persistent pain and limited mobility, severely affecting a patient's quality of life.[1] Despite the remarkable self-healing ability of bones, defects that exceed a certain critical size fail to regenerate spontaneously, resulting in nonunion and loss of function.[2] Traditional treatments, such as autografting and allografting, have shown some clinical success; however, limitations, including donor site constraints, significant surgical trauma, and the potential for immune rejection, continue to pose substantial challenges to their broader clinical use.[3,4] With advancements in tissue engineering technologies, biomaterial scaffolds have emerged as a novel clinical solution, addressing the limitations of autografts.[5] Nevertheless, bone defect repair is a complex process involving immune responses. When biomaterial scaffolds are implanted, they initially interact with immune cells, triggering a foreign body reaction that may adversely affect subsequent bone tissue healing and remodeling processes.[6] Scaffolds that create a favorable immune micro-environment can facilitate interactions between host cells and biomaterials, thereby promoting effective bone regeneration.[7] Therefore, the development of innovative multifunctional biomaterials with immunomodulatory capabilities has become a key focus for improving the success rate of bone defect repair.

Recent research in bone immunology has shown that the complex interactions between biomaterials and host cells are crucial determinants of the fate of the implanted biomaterial.[8,9] Following biomaterial scaffold implantation, changes in the immune micro-environment play a critical role in osteogenesis,[10] although excessive inflammation can result in delayed bone healing, poor bone integration, and complications such as implant failure.[11] As key participants in immune responses to biomaterials, macrophages exhibit significant potential in the regulation of immune responses and osteogenesis in bone defect areas.[12] Macrophages display remarkable plasticity and diversity, allowing them to differentiate into various phenotypes under different stimuli, typically manifesting as M1 and M2 phenotypes.[13] To combat infection and inflammation, macrophages are activated into classical M1 macrophages, which secrete a variety of proinflammatory factors, including interleukin (IL) 1β, tumor necrosis factor-α (TNF-α), and inducible nitric oxide synthase (iNOS), to promote bone remodeling.[14] However, these factors amplify the foreign body reaction, eventually leading to chronic inflammation.[15] In contrast, selectively activated M2 macrophages produce various anti-inflammatory cytokines, such as IL-10, arginase-1, transforming growth factor-β, and bone morphogenetic protein-2 (BMP-2), to alleviate inflammation, repair damaged tissues, promote extracellular matrix synthesis, and enhance osteogenesis.[9,16] Owing to their inherent plasticity, macrophages can switch between different functional phenotypes in various micro-environments.[17] M1 macrophages can convert to M2 macrophages in response to tissue healing stimuli, whereas M2 macrophages can be reprogrammed into M1 macrophages in response to inflammatory signals.[18] Therefore, the exploration and rational design of scaffold materials capable of modulating macrophage polarization hold great promise for enhancing the bone regenerative performance of biomaterials.

Polycaprolactone (PCL), a common synthetic polymer, has been widely applied in the biomedical field due to its excellent biocompatibility and biodegradability. However, PCL-based scaffolds face challenges such as slow degradation rates, poor mechanical properties, and low cell affinity, which limit their use in tissue engineering applications.[19] To address these issues, surface modification strategies of PCL scaffolds, such as incorporating ceramic materials or other biopolymers to enhance hydrophilicity and promote cell adhesion and proliferation, have been proposed. Nevertheless, challenges such as mechanical property imbalance and limited enhancements in cell proliferation persist.[20,21] After in-depth studies of bone repair materials, inorganic bioceramic materials with multiple biological functions have provided innovative directions for bone regeneration. Among these, montmorillonite nanoclay (NC), a layered aluminosilicate, has been approved by the United States Food and Drug Administration (FDA) for use in various pharmaceutical products.[22] Research has shown that NC exhibits an excellent ability to induce osteogenic differentiation, significantly upregulates osteogenic-specific genes such as Runt-related transcription factor 2 (*RUNX2*), osteocalcin, and osteopontin, and provides unique mechanical enhancement properties, making it an ideal modifier to improve the mechanical properties of polymer scaffolds.[23] The interlayer cation hydration effects and hydrogen bonding interactions of the surface hydroxyl groups endow NC with strong natural hydrophilicity.[24] During composite formation, NC can overcome the limitations of traditional fillers by retaining its original biological activities within the polymer matrix.[25] Studies have shown that NC enhances bone regeneration by modulating immune responses and promoting cell differentiation.[26] When combined with PCL, NC has the potential to improve the inherent hydrophobicity of PCL and endow the resulting material with excellent biological activity. However, few studies have reported the considerable therapeutic effect of NC/PCL electrospun

materials in wound healing applications,[27,28] and research on the use of NC/PCL scaffolds for immunoregulation and bone repair remains limited.

Hydroxyapatite (HA), the main inorganic component of bone, demonstrates good biocompatibility[29]; however, its clinical use is limited by mechanical brittleness and insufficient inherent osteoinductive activity.[30] HA/PCL composite scaffolds exhibit good bone repair potential,[31] yet their osteoinductive capability still falls short of the biological requirements for optimal bone regeneration.[32] Although increasing the HA content can enhance the osteoinductive potential of the scaffolds, it also significantly increases the material's brittleness, which is unfavorable for its application in bone repair.[33] Recent studies have revealed that the generation of HA composites or HA surface modification can activate the innate immune system during the early stages of bone healing by stimulating macrophages, inducing cytokine and osteogenesis-related factor secretion, and promoting bone tissue regeneration.[34] Notably, researchers have reported that NC/HA composite systems exhibit synergistically enhanced effects, and when combined with chitosan, the final composite demonstrates significantly improved mechanical properties, cytocompatibility, antibacterial activity, and cellular response regulation.[35–37] We hypothesize that constructing HA/NC/PCL composite scaffolds will not only retain the excellent mechanical strength of the scaffold but also significantly enhance its biological activities, such as immunoregulation and bone regeneration. However, research on the construction of such composite systems with PCL and their underlying immune modulation mechanisms remains limited.

Therefore, in this study, three-dimensional (3D) printing technology was used to construct a synergistically enhanced HA/NC-modified PCL composite scaffold. Its biocompatibility, mechanical strength, and effects on macrophage polarization in the bone immune microenvironment were evaluated both *in vitro* and *in vivo* to investigate its capacity to promote defect repair. The aim was to develop a composite scaffold with excellent immunoregulation and bone repair performance, addressing a research gap in this field and providing new strategies for the use of 3D-printed PCL-based scaffolds in bone defect repair (Figure 1).

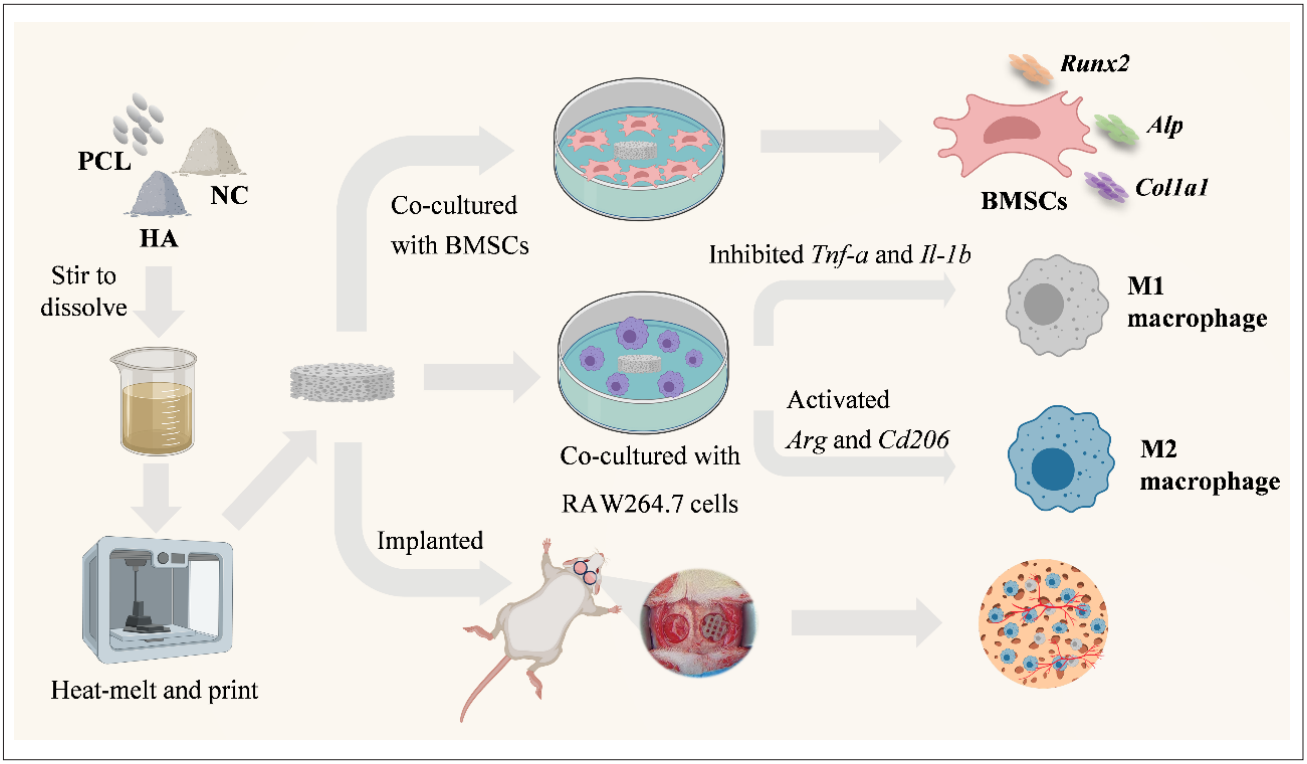

Figure 1. Schematic illustration of the study design. Abbreviations: ALP: Alkaline phosphatase; ARG: Arginase; BMSCs: Bone marrow mesenchymal stem cells; CD206: Cluster of differentiation 206 (mannose receptor); COL1: Type I collagen; HA: Hydroxyapatite; IL: Interleukin; NC: Nanoclay; P: Polycaprolactone; Runx2: Runt-related transcription factor 2; TNF: Tumor necrosis factor.

2. Materials and methods

2.1. Materials

PCL (molecular weight: 54,000) was purchased from Jinan Daigang Biotechnology Co., Ltd. (China). The raw NC (commercially known as Cloisite®Na) with a cation exchange capacity of 92.6 meq/100 g, was obtained from Southern Clay Products, Inc. (United States). The Ultrapure RNA Kit, HiFiScript cDNA (complementary DNA) Synthesis Kit, and UltraSYBR Mixture (Low ROX) were purchased from CWBIO (China). The alkaline phosphatase (ALP) assay kit, bicinchoninic acid (BCA) protein assay kit, and radioimmunoprecipitation assay lysis buffer were provided by Biotain Biotechnology Co., Ltd. (China). Dulbecco's Modified Eagle's Medium (DMEM), fetal bovine serum, penicillin–streptomycin solution, phosphate-buffered saline (PBS), trypsin, and cell-counting kit-8 (CCK-8) assay kit were purchased from Gibco (United States). Rat bone marrow mesenchymal stem cells (BMSCs) and macrophages (RAW264.7) were obtained from Gibco (United States) and American Type Culture Collection (United States). IL-10 (EM220162, BYabscience, China), IL-12 (EM220166, BYabscience, China), rabbit anti-iNOS$^+$ antibody (GB11119, Servicebio, China), and rabbit anti-cluster of differentiation (CD) 163$^+$ antibody (GB15340, Servicebio, China) were used, along with their corresponding secondary antibodies labeled with horseradish peroxidase (HRP)-conjugated goat anti-rabbit IgG (GB23303, Servicebio, China). Anti-BMP-2 antibody (bs-1012R, Bioss, China) was used with a corresponding secondary antibody labeled with Alexa Fluor 488-conjugated goat anti-rabbit IgG (bs-1012R, Bioss, China). An anti-vascular endothelial growth factor (VEGF) antibody (GB15165, Servicebio, China) was also employed.

2.2. Fabrication of nanoclay/polycaprolactone and hydroxyapatite/montmorillonite nanoclay/polycaprolactone scaffolds

NC powder (250 mg) and a mixture of HA (100 mg) with NC (250 mg) were separately dissolved in 10 mL dichloromethane solution containing 1 g PCL. After thorough stirring, the mixtures were poured into corresponding glass dishes and left to evaporate the dichloromethane, yielding the raw materials for the nanoclay/polycaprolactone (NP) and hydroxyapatite/montmorillonite nanoclay/polycaprolactone (HNP) scaffolds. These raw materials were then placed into the feed barrel of a 3D printer (EFL-BP-6603, Suzhou Intelligent Manufacturing Institute, China), where they were heated to a melting point. The nozzle diameter was set at 0.25 mm, the barrel temperature was 75°C, and the nozzle temperature was 80°C. Fiber spacing was 0.8 mm × 0.8 mm, print speed was 10 mm/s, and fiber orientation ranged from 0° to 90°, with an air pressure of 400 kPa. The scaffold layer height was set at 80% of the nozzle diameter. Cylindrical 3D scaffolds were printed, with those intended for mechanical strength testing having a diameter of 10 mm and a height of 5 mm, while scaffolds for performance and cell experiments measured 5 mm in diameter and 1 mm in height.

2.3. Surface characterization of scaffolds

2.3.1. Surface morphology analysis

The surface morphology and structure of the P (polycaprolactone), NP, and HNP scaffolds were characterized using a high-resolution field emission scanning electron microscope (SEM; Merlin, Zeiss, Germany) and a transmission electron microscope (TEM; JEM-2100HR, JEOL, Japan).

2.3.2. Composition analysis

Thermogravimetric analysis was conducted to measure the thermal weight loss of the scaffolds. The samples were heated from room temperature to 800°C at a rate of 10°C per minute under a nitrogen atmosphere.

2.3.3 Determination of scaffold porosity

The dry mass of the scaffold sample was measured as M_0. The total mass of a pycnometer containing anhydrous ethanol at room temperature was recorded as M_1. The sample was then placed in the pycnometer, subjected to ultrasonic treatment for 10 min to remove bubbles, and the total mass of the sample was recorded as M_2. After removing the sample, the remaining mass was measured as M_3. The porosity of the scaffold was calculated using the following formula:

$$P = \frac{(M_2 - M_3 - M_0)}{(M_1 - M_3)} \quad \text{(I)}$$

2.3.4 Hydrophilicity test of the scaffolds

A 2 μL drop of ultrapure water was gently added to the surface of the sample using a micro-injector, and the droplet deposition process was recorded using a high-resolution camera. The dynamic contact angle between the droplet and the scaffold surface was measured using a contact angle goniometer.

2.3.5 Mechanical strength test of the scaffolds

The mechanical properties of the scaffolds were analyzed using an INSTRON testing machine (345C-S, United States). At room temperature, the height of each scaffold was measured using a vernier caliper before being placed on the testing platform. The extrusion speed was set to 5

mm/min, and the test was terminated when the scaffold reached 80% compressive deformation. During the compression phase, the pressure value was recorded as the compressive strength of the scaffold.

2.4. Cell experiments

2.4.1. Cell culture and scaffold sterilization

BMSCs and RAW264.7 cells were cultured after resuscitation in a thermostatic cell culture incubator (MCO-18AIC, PHCbi, Japan) at 37°C with 5% CO_2. The complete culture medium consisted of a high-glucose DMEM medium supplemented with 10% fetal bovine serum, 100 μg/mL penicillin, and 100 μg/mL streptomycin. The medium was replaced daily or every 2 days, depending on cell condition. Cells were passaged upon reaching 70%–80% confluence, and only cells at passages 3–5 were used for further experiments.

Prior to the experiment, scaffolds from each group were immersed in 75% ethanol for 2 h. Afterward, the scaffolds were rinsed three times with PBS and sterilized overnight in an ultraviolet disinfection cabinet (Shengzhiyuan and Kejia Education Equipment Co., Ltd., China).

2.4.2 Assessment of scaffold biocompatibility

The biocompatibility of the scaffolds with BMSCs was evaluated. Briefly, sterilized scaffold samples were placed in 48-well plates, and 5×10^4 BMSCs were seeded onto the samples. After culturing for 1, 3, and 7 days, the culture medium was removed, and cell proliferation on the different scaffolds was assessed using a CCK-8 assay kit. Optical density values were measured using a microplate reader (TecanSpark, Austria).

Cell viability was determined by live/dead cell staining. The morphology and distribution of cells on the scaffold surface were observed using an inverted fluorescence microscope. After 72 h of cell adhesion and proliferation on the scaffold surface, selected cells were subjected to further testing.

2.4.3 Evaluation of scaffold-induced osteogenic differentiation and macrophage polarization

ALP staining was performed to evaluate ALP activity after 7 days of the osteogenic differentiation induction. After the removal of osteogenic medium, cells were washed twice with PBS, fixed with 4% paraformaldehyde for 2 min, and washed again with PBS. Subsequently, BCIP/NBT substrate solution (250 μL/cm^2; Sigma-Aldrich) was added to each well and incubated at room temperature for 4 h. The wells were then washed with PBS to remove the substrate solution, immersed in 1 mL of distilled water, and observed under an optical microscope.

Four groups of irradiated (10 kGy) sterilized scaffolds were placed in well plates and co-cultured with BMSCs, with the osteogenic induction medium replaced every other day. After 7 days of co-culture, ALP activity in each sample was measured using an ALP assay kit. Total cellular protein was quantified using the BCA assay.

BMSCs (1×10^5) were seeded into 48-well plates containing scaffold samples. The osteogenic induction medium was prepared using DMEM complete medium (100 mL complete medium + 0.39 mg dexamethasone + 1.76 mg vitamin C + 306.11 mg β-glycerophosphate sodium), with regular medium changes. Osteogenic induction was terminated on days 7 and 14, and quantitative reverse transcription polymerase chain reaction (qRT-PCR) was used to detect the expression of osteogenic marker genes *Alp*, *Runx2*, and *Col1a1*, using *Gapdh* as the internal control gene.

RAW264.7 cells were seeded onto scaffold samples in 48-well plates at a density of 5×10^4 cells per well. The complete culture medium was replaced every 2–3 days. The culture medium from each group was collected, mixed with osteogenic induction medium in a 1:5 ratio, and used as a macrophage polarization medium. On days 1 and 3, the expression levels of M1 immune marker genes, including *Tnfa* and *Il1b*, as well as M2 immune marker genes, such as *Cd206* and *Arg*, were determined using qRT-PCR, with *Gapdh* as the internal control. The specific primers used for the target genes are listed in Table 1.

2.4.4 Enzyme-linked immunosorbent assay

The levels of IL-12 and IL-10 in the macrophage-conditioned medium of the scaffolds were assessed using enzyme-linked immunosorbent assay (ELISA) kits according to the manufacturer's instructions. Standard, zero, blank, and sample wells were prepared on the plate. In the standard wells, 50 μL of standard solutions at varying concentrations were added, while 50 μL of sample diluent was added to the zero wells. The blank wells were left empty, and 50 μL of test samples were added to the sample wells. Excluding the blank wells, 100 μL of HRP-conjugated detection antibody was added to the standard, zero, and sample wells. The reaction plate was sealed with a sealing film and incubated in the dark at 37°C for 60 min. After incubation, the plate was washed five times. Subsequently, substrates A and B were thoroughly mixed in a 1:1 volume ratio, and 100 μL of the resulting substrate mixture was dispensed into each well. The reaction plate was sealed again and incubated in the dark at 37°C for 15 min. Finally, 50 μL of stop solution was added to each well, and absorbance (optical density) was measured at 450 nm using a microplate reader.

Table 1. Specific primers used for genes involved in osteogenesis and macrophage polarization

Gene transcript	Forward primer sequence (5'–3')	Reverse primer sequence (5'–3')
Runx2	TCGGAGAGGTACCAGATGGG	AGGTGAAACTCTTGCCTCGT
Col1a1	TTCTCCTGGCAAAGACGGAC	CTCAAGGTCACGGTCACGAA
Alp	GGAGATGGTATGGGCGTCTC	GGACCTGAGCGTTGGTGTTA
Cd206	ATGGATGTTGATGGCTACTGG	TTCTGACTCTGGACACTTGC
Arg	TGGACAGACTAGGAATTGGCA	CCAGTCCGTCAACATCAAAACT
Tnfa	GAGGCCAAGCCCTGGTATG	CGGGCCGATTGATCTCAGC
Il1b	TACAGGCTCCGAGATGAACA	AGGCCACAGGTATTTTGTCG
Gadph	GCCATGAGGTCCACCACCCT	AAGGTCATCCCAGAGCTG

2.5. Animal experiments

Male Sprague–Dawley (SD) rats (eight weeks of age; total rats in the study = 42) were used to establish bilateral calvarial defects for *in vivo* investigation. The rats were randomly assigned to one of the following groups: control (Con)-Con, Con-P, Con-NP, Con-HNP, P-NP, P-HNP, and NP-HNP (n = 6 per group). Bilateral calvarial defect models were created for all rats, and the respective scaffolds were implanted according to group assignments. In each rat, one side of the calvaria served as a Con, corresponding to a sham surgery. The group designations were defined as follows:

- Con-Con: both sides received sham surgery (no scaffold implantation);
- Con-P: one side received sham surgery, the other received a PCL scaffold;
- Con-NP: one side received sham surgery, the other received an NP scaffold;
- Con-HNP: one side received sham surgery, the other received an HNP scaffold;
- P-NP: one side received a PCL scaffold, the other received an NP scaffold;
- P-HNP: one side received a PCL scaffold, the other received an HNP scaffold;
- NP-HNP: one side received an NP scaffold, the other received an HNP scaffold.

2.5.1. Preparation of bilateral calvarial defects in Sprague–Dawley rats

Prior to surgery, all SD rats underwent a fasting period of 12 h and water deprivation for 8 h. The three scaffold types were pre-incubated overnight in high-glucose DMEM complete medium (containing 10% serum, 100 μg/mL penicillin, and 100 μg/mL streptomycin) 1 day before the procedure. Anesthesia was induced via intraperitoneal injection of a mixture containing 8% chloral hydrate and 20% urethane. Following successful anesthesia induction, the calvarial area was shaved, and the rats were secured in a prone position on the operating table. The surgical area was disinfected with 1% iodine tincture and covered with sterile drapes. A 2 cm incision was made along the midline of the skull, and the subcutaneous and periosteal tissues were gently separated using a scalpel handle to expose the bilateral parietal bones, occipital bone, and part of the frontal bone. A dental drill was used to create bilateral full-thickness bone defects, each 5 mm in diameter, along the calvarial midline. According to the experimental group assignments, scaffolds were implanted into the calvarial defects, while the blank control group received no scaffold implantation (Figure 2). The muscle and skin layers were closed using biodegradable absorbable sutures. Postoperatively, the animals were returned to their cages and monitored under standard housing conditions. Penicillin (800,000 U/day) was administered via intramuscular injection for 3 consecutive days. All rats resumed normal diet and activity within 3 days, and no wound infection was observed. Rats were euthanized at weeks 4, 8, and 12 post-implantation. Calvarial bone specimens were harvested and fixed in 4% paraformaldehyde for micro-computed tomography (CT) analysis and histological evaluation.

To assess systemic biocompatibility, blood samples were collected for hematological analysis. In addition, major organs including the heart, liver, spleen, lungs, and kidneys were harvested and subjected to hematoxylin and eosin (H&E) staining for histopathological examination.

2.5.2. Micro-computed tomography scanning and data analysis

Calvarial specimens containing defect sites were harvested at 4, 8, and 12 weeks post-implantation and fixed in 4% paraformaldehyde for 24 h. Micro-CT images were acquired using a micro-CT scanner (ZKKS-MCT-Sharp, China), with specimens fixed along the longitudinal axis in the holder. The scanning parameters were set as follows:

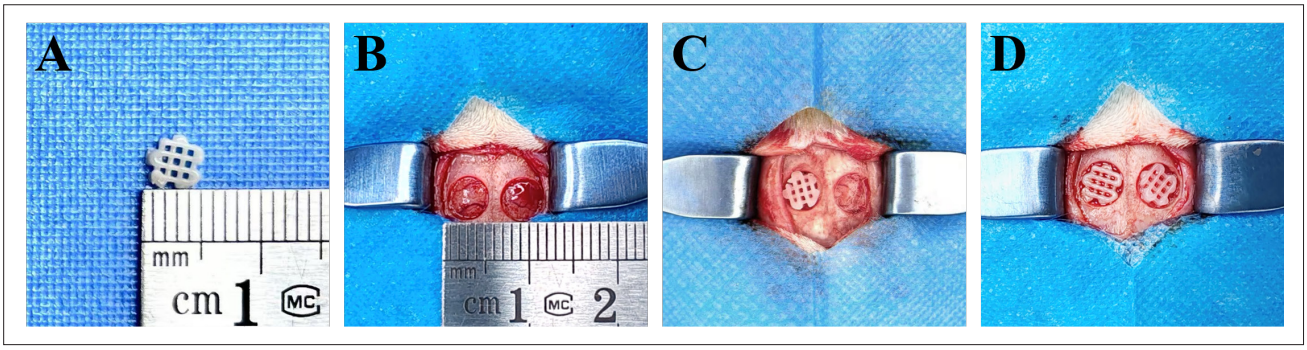

Figure 2. Establishment of the calvarial defect model in Sprague–Dawley rats and scaffold implantation. (A) Gross morphology of the fabricated scaffold; (B) Schematic of the bilateral critical-sized calvarial defect model in rats (5 mm in diameter, 1 mm in thickness); (C) Unilateral implantation of the scaffold into one defect site; (D) Bilateral implantation of scaffolds into both defect sites.

voltage, 70 kV; power, 7 W; frame averaging, 4; angular increment, 0.72°; and exposure time, 100 ms. A full 360° rotation was completed for each specimen. Micro-CT data were analyzed using bone-analysis software (CTAn, Bruker, version 2.0, China) to quantify total volume (TV), bone volume (BV), bone volume fraction (BV/TV), and bone mineral density (BMD).

2.5.3. Histological analysis

Following micro-CT scanning, calvarial specimens were decalcified in ethylenediaminetetraacetic acid solution at 4°C for 35 days. After decalcification, samples were harvested from the center of the defect, embedded in paraffin, and sectioned into 5 μm-thick slices. Tissue sections were stained using H&E and Masson's trichrome staining kits, following the manufacturer's instructions. Stained sections were imaged using a fluorescence microscope (NIKON ECLIPSE C1, Nikon, Japan).

Immunofluorescence staining was performed on two consecutive sections from each sample to determine macrophage phenotypes. After PBS washing, sections were blocked with goat serum and incubated overnight at 4°C with anti-iNOS (1:2500), a marker for M1 macrophages. After incubation with the appropriate secondary antibody, tyramide signal amplification dye was applied and incubated for 10 min in the dark. Antigen retrieval was then performed using microwave treatment in an antigen retrieval buffer. Sections were subsequently incubated with anti-CD163 (1:2000), a marker for M2 macrophages, followed by the corresponding secondary antibody. Nuclei were counterstained with 4',6-diamidino-2-phenylindole (DAPI).

For the detection of osteogenic and angiogenic markers, sections were blocked with 10% donkey serum and incubated overnight at 4°C in a humidified chamber with a mixed solution of anti-BMP-2 (1:1:200) and anti-VEGF (1:1000) primary antibodies. Appropriate secondary antibodies were applied and incubated for 50 min in the dark. Nuclei were counterstained with DAPI.

2.6. Statistical analysis

Experimental data are expressed as mean ± standard deviation. All statistical analyses were performed using GraphPad Prism software. One-way analysis of variance followed by Dunnett's multiple comparison test was used to determine statistical differences between groups. A p-value < 0.05 was considered statistically significant.

3. Results

3.1. Preparation and characterization of the scaffolds

The surface morphology of the 3D-printed PCL, NP, and HNP scaffolds was examined using SEM, as shown in Figure 3A. Compared with the P scaffold, the NP scaffold exhibited markedly fewer surface pores. In contrast, the HNP scaffold presented an increased number of pores relative to the NP scaffold. NC particles were clearly observed on the NP scaffold surface, accompanied by increased surface roughness and reduced pore size. In the HNP scaffold, although the overall surface morphology and pore size were similar to those of the P scaffold, a notable increase in the number of attached NC particles was observed at higher magnification (see micrographs in Figure 3A with a scale bar of 30 μm).

When implanted *in vivo*, scaffold hydrophilicity plays a key role in modulating cell behavior, as hydrophobic surfaces tend to hinder cell adhesion and migration, whereas hydrophilic surfaces promote cell proliferation and bone tissue regeneration.[38] Water contact angle measurements were subsequently conducted using the sessile drop method (Figure 3B1 and 3B2). The P scaffold exhibited the highest contact angle, indicating strong hydrophobicity. Compared

with the P scaffold, the NP scaffold demonstrated a slightly lower contact angle, whereas the HNP scaffold showed a significant reduction in contact angle ($p < 0.001$), indicating enhanced hydrophilicity.

Thermogravimetric analysis was performed to assess the thermal stability of each scaffold (Figure 3C). The total mass losses for the P, NP, and HNP scaffolds were 99.88%, 79.61%, and 77.40%, respectively, corresponding to the increased proportions of NC and HA. The remaining inorganic content in each group was consistent with the expected loading ratios of NC and HA.

The porosities of the P, NP, and HNP scaffolds were calculated using a gravimetric method (Figure 3D), yielding values of 68.08 ± 1.73%, 64.93 ± 0.91%, and 65.79 ± 1.90%, respectively. Owing to the consistent amount of PCL and identical 3D printing parameters, no significant differences in porosity were observed among the three groups ($p > 0.05$).

The mechanical properties of the P, NP, and HNP scaffolds were also evaluated (Figure 4). The compressive strengths of the P, NP, and HNP scaffolds were 5.62 ± 1.47 MPa, 17.47 ± 0.45 MPa, and 11.88 ± 0.90 MPa, respectively. The corresponding compressive moduli were 1166.30 ± 384.71 MPa, 3429.39 ± 68.42 MPa, and 3048.92 ± 124.53 MPa, respectively. These results demonstrate that the incorporation of NC significantly enhances the mechanical properties of the scaffolds. Compared with

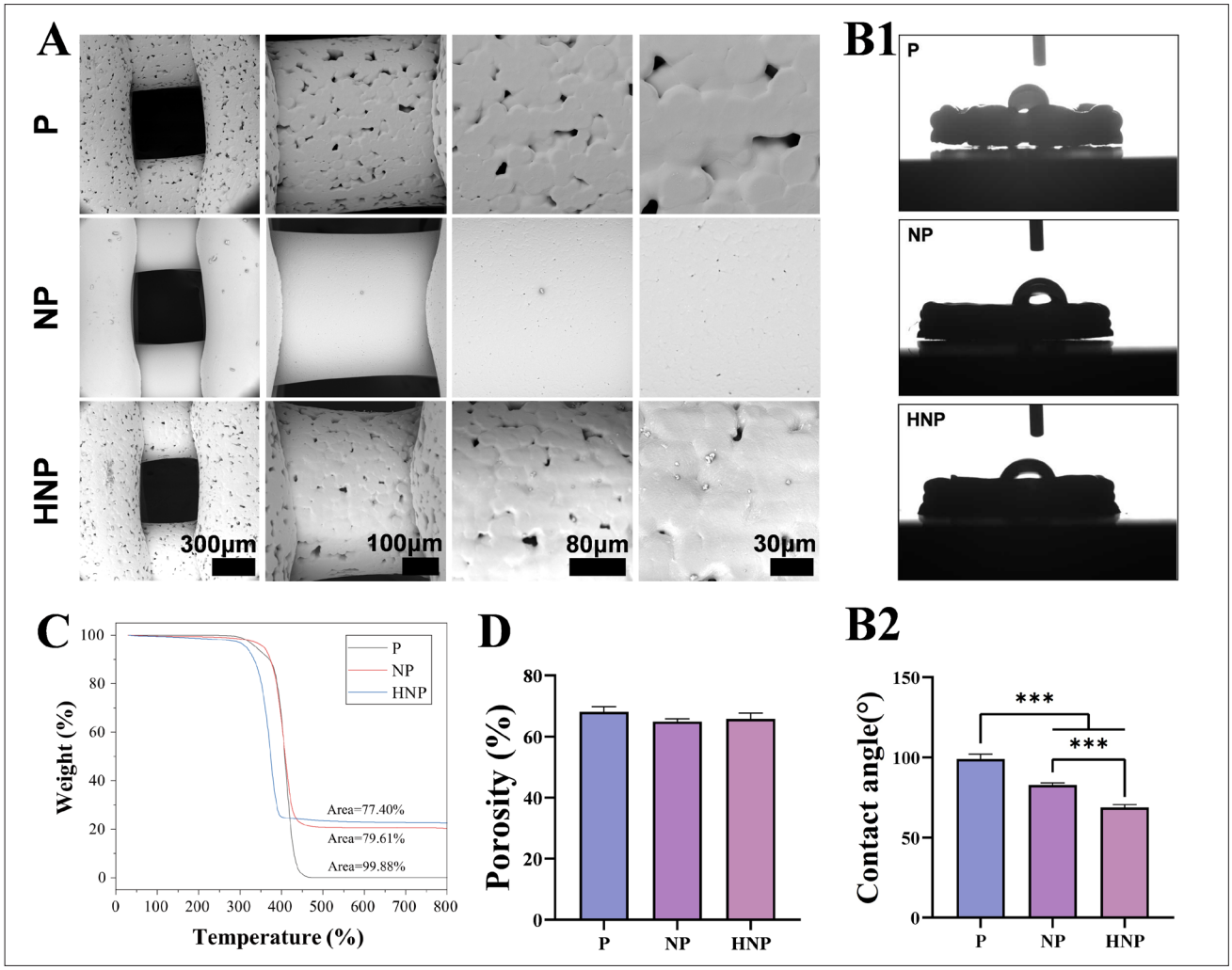

Figure 3. Fabrication and characterization of the three types of scaffolds. (A) Scanning electron microscope images of the P, NP, and HNP scaffolds at different magnifications (magnifications: 200×, 500×, 1000×, and 2000×, scale bars: 300 μm, 100 μm, 80 μm, and 30 μm). (B1, B2) Representative images of water contact angles and comparison of scaffold hydrophilicity. (C) Thermogravimetric analysis curves of the scaffolds. (D) Comparison of scaffold porosity among groups. Note: ***$p < 0.001$. Abbreviations: HNP: Hydroxyapatite/montmorillonite nanoclay/polycaprolactone; NP: Nanoclay/polycaprolactone; P: Polycaprolactone.

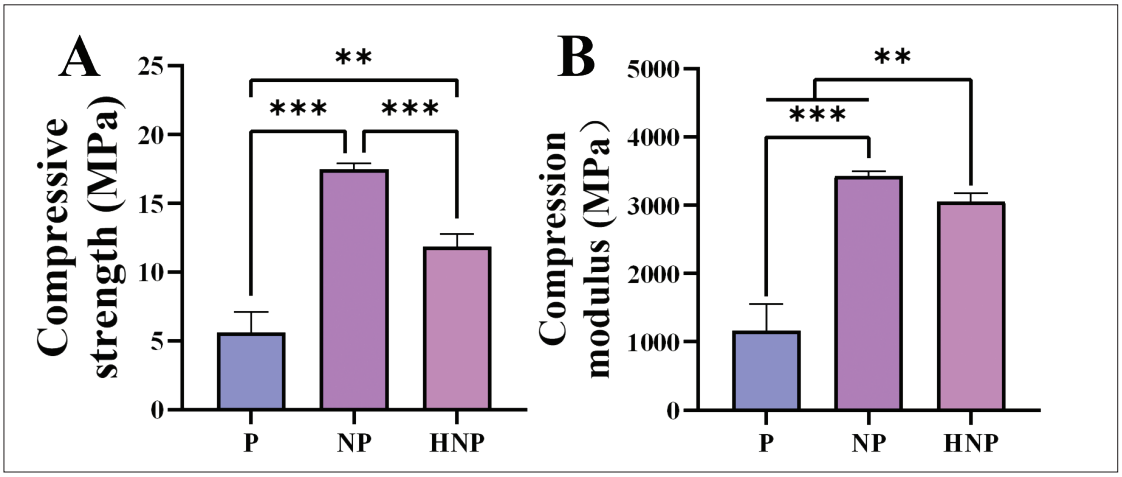

Figure 4. Comparison of compressive strength and compressive modulus of the scaffolds. Notes: $^{**}p < 0.01$, $^{***}p < 0.001$. Abbreviations: HNP: Hydroxyapatite/montmorillonite nanoclay/polycaprolactone; NP: Nanoclay/polycaprolactone; P: Polycaprolactone.

the HNP scaffold, the NP scaffold exhibited significantly greater compressive strength and modulus ($p < 0.05$).

3.2. *In vitro* evaluation of scaffold biocompatibility, promotion of osteogenic differentiation, and regulation of macrophage polarization

3.2.1. Cell proliferation and adhesion analyses

Cell viability on the 3D-printed P, NP, and HNP scaffolds was assessed using the CCK-8 assay. BMSC proliferation on the scaffolds was measured after days 1, 3, and 7 of co-culture. As shown in Figure 5A, no significant differences in BMSC proliferation were observed among the three groups on day 1. By day 3, both the NP and HNP groups exhibited significantly higher BMSC proliferation compared to the P group. However, the difference between the HNP and NP groups was minimal. By day 7, BMSC proliferation in the HNP group was significantly greater than in both the P and NP groups ($p < 0.05$).

Cell adhesion and proliferation are critical factors in scaffold functionality. To evaluate cell activity on each scaffold, BMSCs were co-cultured with the P, NP, or HNP scaffolds for 3 days, and cell viability was assessed using live/dead staining. As shown in Figure 5B, significantly more BMSCs adhered to the HNP scaffold than to the P and NP scaffolds, with minimal attachment observed on the P scaffold. These results were consistent with the findings from the CCK-8 assay, which demonstrated significantly higher BMSC viability on the HNP scaffold compared to the other two groups.

3.2.2. Promotion of osteogenic differentiation potential

The osteogenic differentiation of stem cells on different scaffold surfaces was evaluated using ALP staining and activity assays. As shown in Figure 6A, after 7 days of co-culture, the PCL scaffold alone did not significantly promote osteogenic differentiation, as indicated by sparse and faint ALP staining. In contrast, the NP scaffold, which contained NC, exhibited noticeably more ALP staining, while the HNP scaffold, incorporating both NC and HA, showed even more pronounced ALP staining.

As depicted in Figure 6B, ALP activity in the HNP group was significantly higher than in the P and NP groups ($p < 0.001$). Additionally, the expression levels of osteogenesis-related genes (*Alp*, *Col1a1*, and *Runx2*) were assessed on days 7 and 14 to evaluate the osteogenic differentiation of BMSCs on each scaffold. As shown in Figure 6C–E, the HNP group demonstrated significantly upregulated expression of osteogenic markers at both time points compared with the other groups ($p < 0.05$). Thus, the HNP scaffold exhibited significantly enhanced osteogenic induction relative to both the P and NP scaffolds.

3.2.3. Immunomodulation in vitro

The immune micro-environment surrounding the grafts plays a critical role in the bone regeneration process. To systematically evaluate the effects of different scaffolds on macrophage polarization and immune modulation, RAW264.7 cells were co-cultured with each scaffold, and the expression of macrophage polarization-related genes was assessed on days 1 and 3. As shown in Figure 7A–D, compared with the P and NP groups, the HNP group exhibited significant upregulation of M2 macrophage-related genes (*Cd206* and *Arg*) and downregulation of M1 macrophage-related genes (*Tnfa* and *Il1b*). On day 3, *Cd206* expression in the HNP group was approximately seven-fold higher than in the P group and two-fold higher than in the NP group. Similarly, *Arg* expression in the HNP

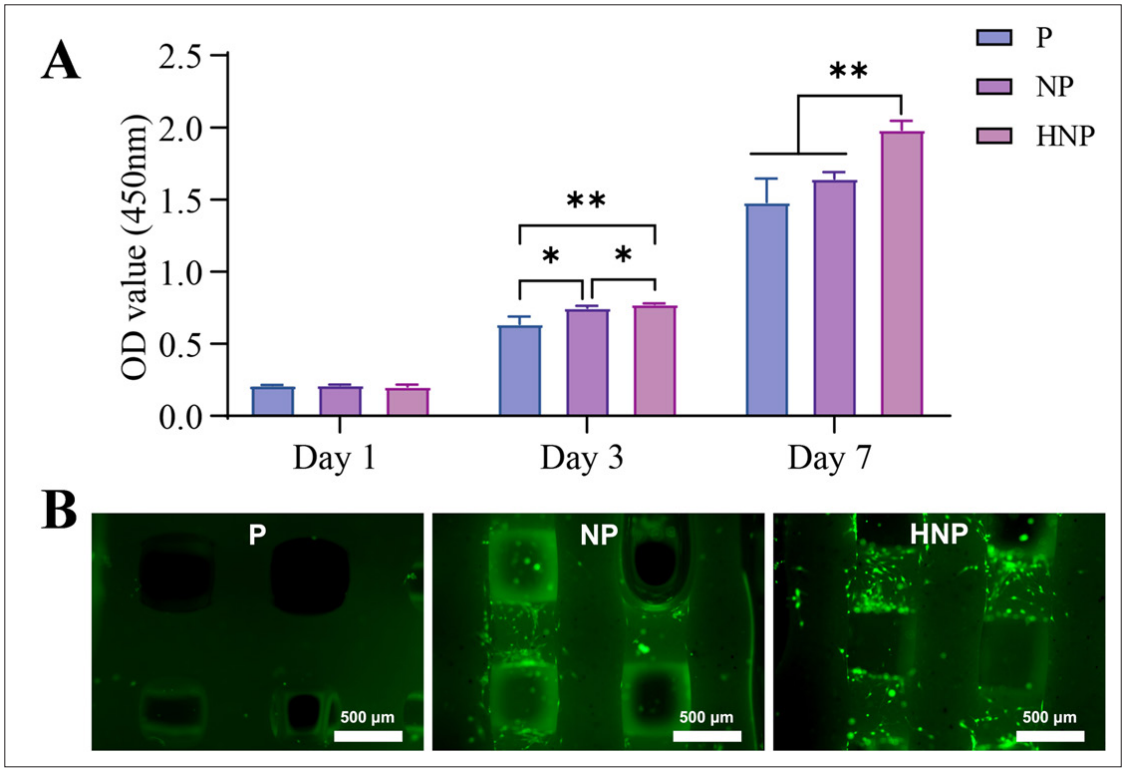

Figure 5. Biocompatibility of the scaffolds. (A) Proliferation and viability of BMSCs on the scaffolds at days 1, 3, and 7 of co-culture. (B) Live/dead staining of BMSCs co-cultured with scaffolds for 3 days. Magnification: 10×; scale bar: 500 μm. Notes: *$p < 0.05$, **$p < 0.01$. Abbreviations: BMSCs: Bone marrow mesenchymal stem cells; HNP: Hydroxyapatite/montmorillonite nanoclay/polycaprolactone; NP: Nanoclay/polycaprolactone; OD: Optical density; P: Polycaprolactone.

group was about eight-fold higher than in the P group and three-fold higher than in the NP group at the same time point. In contrast, *Tnfa* expression in the P and NP groups was six-fold and two-fold higher, respectively, than in the HNP group, while *Il1b* expression was nine-fold and three-fold higher, respectively ($p < 0.05$). To further validate the immunomodulatory effects of the scaffold, the concentrations of the pro-inflammatory cytokine IL-12 and the anti-inflammatory cytokine IL-10 in the culture medium were quantified using an ELISA assay. As shown in Figure 7E and 7F, the HNP scaffold significantly suppressed the pro-inflammatory cytokine IL-12 levels and enhanced the anti-inflammatory cytokine IL-10 levels ($p < 0.05$), consistent with the gene expression (PCR) findings.

3.3. *In vivo* validation of scaffold biocompatibility and osteogenic differentiation

3.3.1. Biocompatibility of the scaffolds

To assess the biocompatibility and safety of the scaffolds, we measured the blood parameters of the SD rats at weeks 4, 8, and 12 post-surgery, as shown in Table 2. No significant differences were observed in white blood cells, red blood cells, hemoglobins, platelets, alanine aminotransferase, aspartate aminotransferase, creatinine, or urea levels among the groups ($p > 0.05$).

At weeks 4, 8, and 12 post-surgery, the heart, liver, spleen, lungs, and kidneys of the rats from each group were harvested and prepared into tissue sections for H&E staining to assess pathological changes and evaluate the cytotoxicity of the scaffolds *in vivo*. As shown in Figures 8–10, no inflammatory cell infiltration was observed in the major organs of the rats from any group, and no significant histopathological differences were noted among the groups.

3.3.2. Micro-computed tomography evaluation

Micro-CT imaging was performed on the SD rat bone defect model at weeks 4, 8, and 12 post-surgery to assess healing in the bone defect area. As shown in Figure 11A, the blank control group, which did not receive a scaffold, exhibited minimal new bone formation during the early postoperative period (weeks 4 and 8), with no significant bone growth observed by week 12. This finding suggests that, without scaffold support, the self-healing capacity of the bone is limited. In contrast, the P group, implanted with pure PCL scaffolds, showed limited new bone

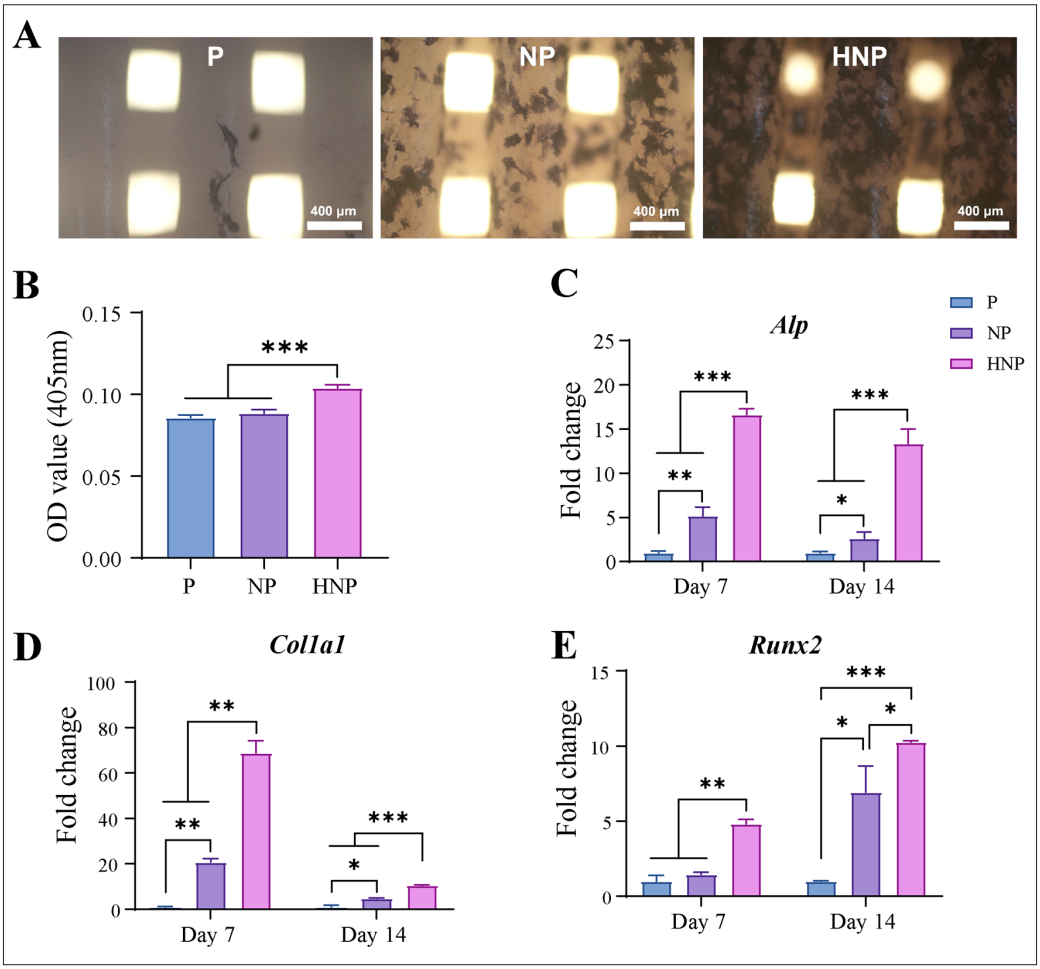

Figure 6. Osteogenic characteristics of the three scaffold groups. (A) ALP staining of the P, NP, and HNP scaffolds after 7 days of co-culture. Magnification: 10×; scale bar: 400 μm. (B) ALP activity on the P, NP, and HNP scaffolds after 7 days of co-culture. (C–E) Expression levels of osteogenesis-related genes (*Alp*, *Col1a1*, and *Runx2*) in BMSCs co-cultured with scaffolds at days 7 and 14. Notes: *$p < 0.05$, **$p < 0.01$, ***$p < 0.001$. Abbreviations: ALP: Alkaline phosphatase; HNP: Hydroxyapatite/montmorillonite nanoclay/polycaprolactone; NP: Nanoclay/polycaprolactone; OD: Optical density; P: Polycaprolactone.

Table 2. Blood indices of rats in each group at weeks 4, 8, and 12 post-surgery

Time point (week)	Clinical test indicators	Group				*p*-value
		Con	P	NP	HNP	
4	WBC (10^9/L)	10.66±1.60	11.65±2.84	12.10±2.57	11.20±2.66	0.9409
	RBC (10^9/L)	8.12±0.49	7.68±0.40	8.06±0.62	7.97±0.57	0.8418
	HB (g/L)	131.50±6.36	146.50±12.02	141.00±9.90	144.00±11.31	0.5392
	PLT (10^9/L)	1006.00±103.24	918.50±84.15	970.50±147.79	854.00±123.04	0.6285
	ALT (U/L)	69.00±1.41	68.00±1.41	64.50±14.85	63.50±13.44	0.9310
	AST (U/L)	108.50±14.85	108.50±17.68	102.00±18.35	103.00±5.66	0.9512
	Urea (mmol/L)	6.56±0.25	5.76±0.59	6.08±1.01	6.54±0.44	0.5850
	Cr (μmol/L)	44.00±12.73	33.50±3.54	41.50±7.78	41.00±5.66	0.6410
8	WBC (10^9/L)	8.16±0.67	8.73±0.70	8.80±1.07	8.62±1.32	0.9092
	RBC (10^9/L)	7.79±1.41	7.57±0.76	7.62±0.13	7.32±0.74	0.9580
	HB (g/L)	132.50±16.26	135.00±9.90	138.50±4.95	127.00±8.49	0.7562

(Continued...)

Table 2. Blood indices of rats (Continued....)

	PLT (10^9/L)	797.50±108.19	714.50±17.68	667.00±41.01	771.50±71.42	0.3528
	ALT (U/L)	60.00±9.90	57.00±4.24	52.50±13.44	50.50±0.71	0.7031
	AST (U/L)	144.50±9.19	145.50±23.33	137.50±20.51	151.50±19.09	0.9006
	Urea (mmol/L)	5.30±1.25	6.63±0.11	6.24±0.11	6.62±0.91	0.3878
	Cr (μmol/L)	38.00±4.24	36.50±3.54	39.50±3.54	37.50±6.36	0.9247
12	WBC (10^9/L)	8.32±0.81	9.13±0.57	8.05±0.35	7.44±4.08	0.8771
	RBC (10^9/L)	7.85±0.19	8.07±0.66	7.87±0.34	8.02±0.21	0.9237
	HB (g/L)	136.50±6.36	140.00±4.24	130.50±3.54	132.00±4.24	0.3064
	PLT (10^9/L)	797.00±118.79	798.00±35.36	861.00±56.57	800.50±54.45	0.7838
	ALT (U/L)	57.00±4.24	55.50±4.95	50.50±9.19	56.00±15.56	0.9031
	AST (U/L)	174.00±22.63	154.50±10.61	160.50±9.19	168.00±8.49	0.5788
	Urea (mmol/L)	7.22±0.18	7.16±0.25	6.64±0.33	6.47±0.14	0.0777
	Cr (μmol/L)	39.00±2.83	40.50±0.71	38.50±2.12	37.00±2.83	0.5578

Abbreviations: ALT: Alanine aminotransferase; AST: Aspartate aminotransferase; Con: Control; Cr: Creatinine; HB: Hemoglobin; HNP: Hydroxyapatite/montmorillonite nanoclay/polycaprolactone; NP: Nanoclay/polycaprolactone; P: Polycaprolactone; PLT: Platelet; RBC: Red blood cell; WBC: White blood cell.

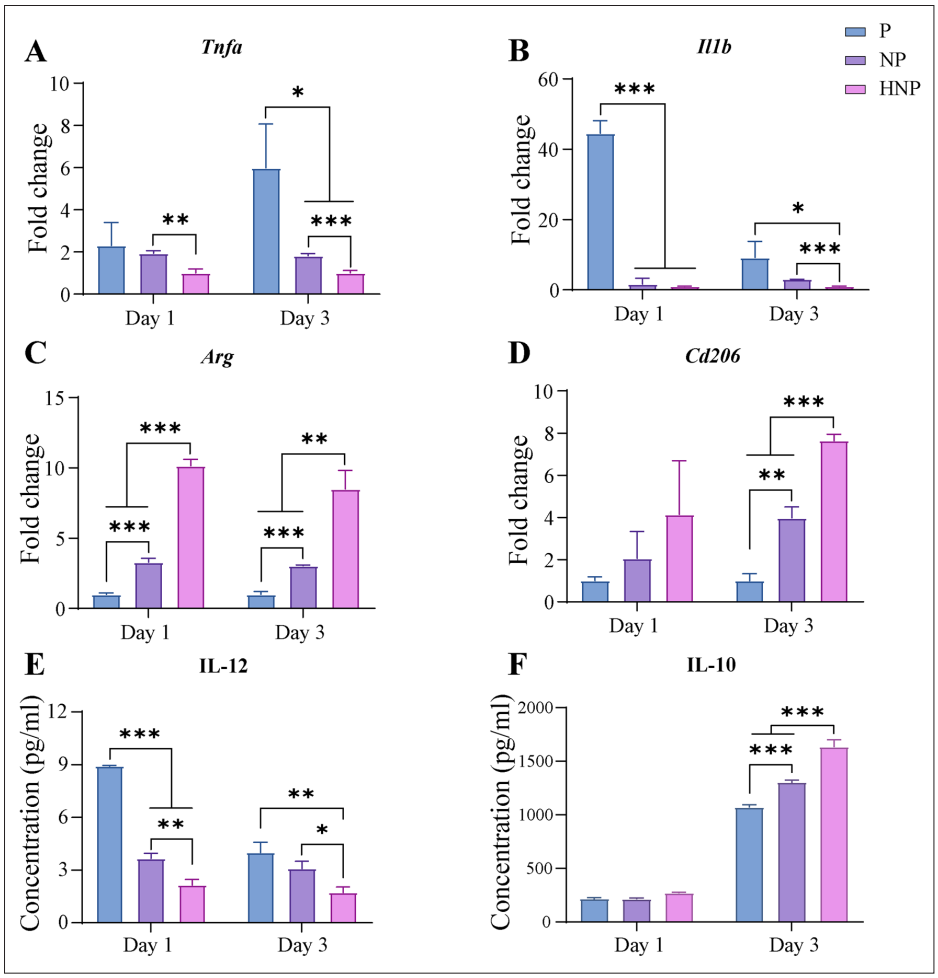

Figure 7. Polarization characteristics of macrophages on the scaffolds. (A–B) Gene expression levels of M1 polarization markers in RAW264.7 cells co-cultured with the scaffolds. (C–D) Gene expression levels of M2 polarization markers in RAW264.7 cells co-cultured with the scaffolds. (E–F) Concentrations of indicated cytokines in RAW264.7 cells co-cultured with the scaffolds. Notes: $^*p < 0.05$, $^{**}p < 0.01$, $^{***}p < 0.001$. Abbreviations: HNP: Hydroxyapatite/montmorillonite nanoclay/polycaprolactone; IL: Interleukin; NP: Nanoclay/polycaprolactone; P: Polycaprolactone.

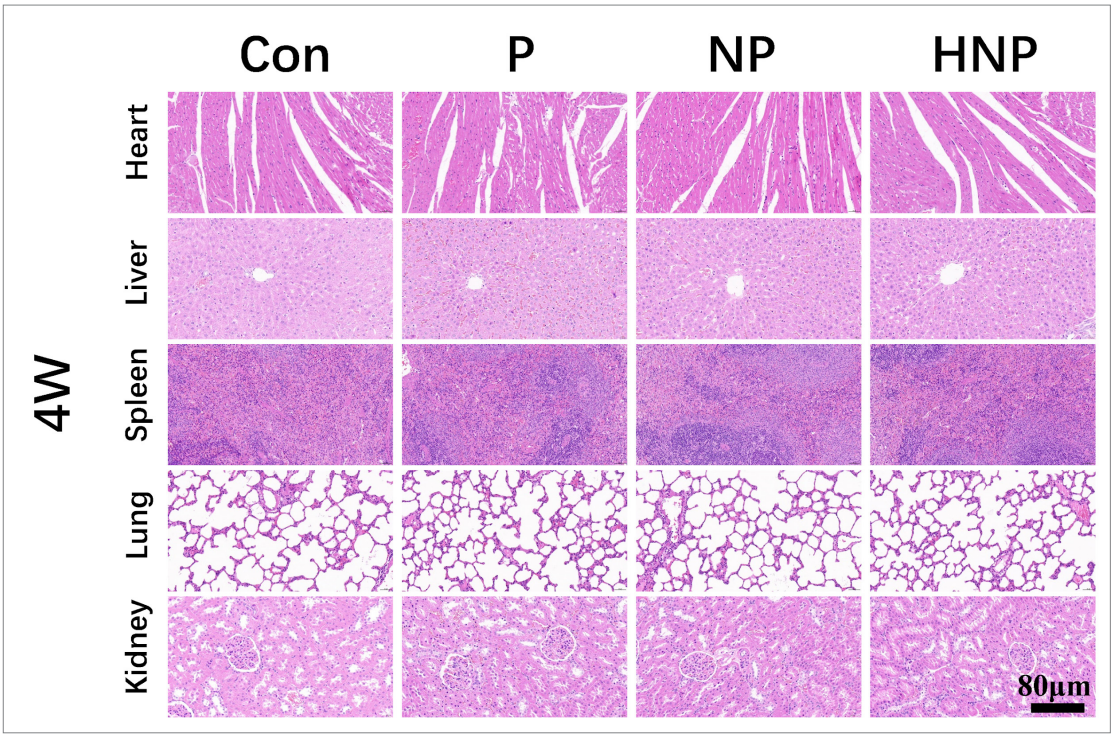

Figure 8. Hematoxylin and eosin staining of the heart, liver, spleen, lung, and kidney of rats at week 4 (4W) post-surgery. Magnification: 40×; scale bar: 80 μm. Abbreviations: Con: Control; HNP: Hydroxyapatite/montmorillonite nanoclay/polycaprolactone; NP: Nanoclay/polycaprolactone; P: Polycaprolactone.

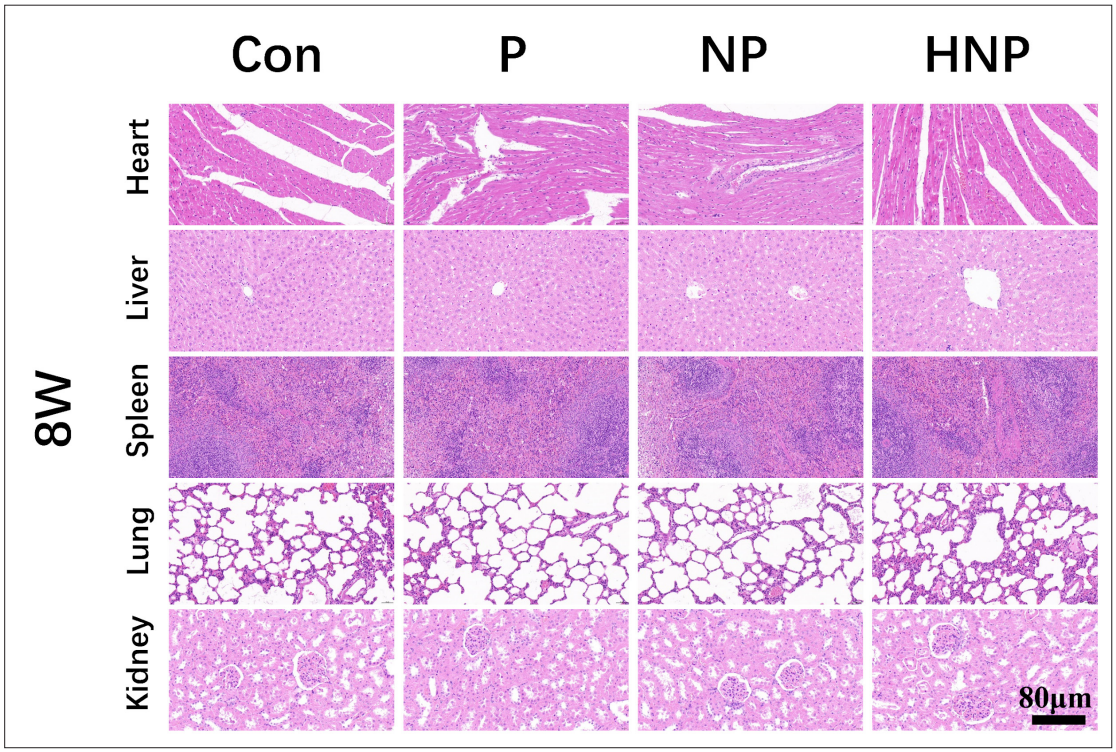

Figure 9. Hematoxylin and eosin staining of the heart, liver, spleen, lung, and kidney of rats at week 8 (8W) post-surgery. Magnification: 40×; scale bar: 80 μm. Abbreviations: Con: Control; HNP: Hydroxyapatite/montmorillonite nanoclay/polycaprolactone; NP: Nanoclay/polycaprolactone; P: Polycaprolactone.

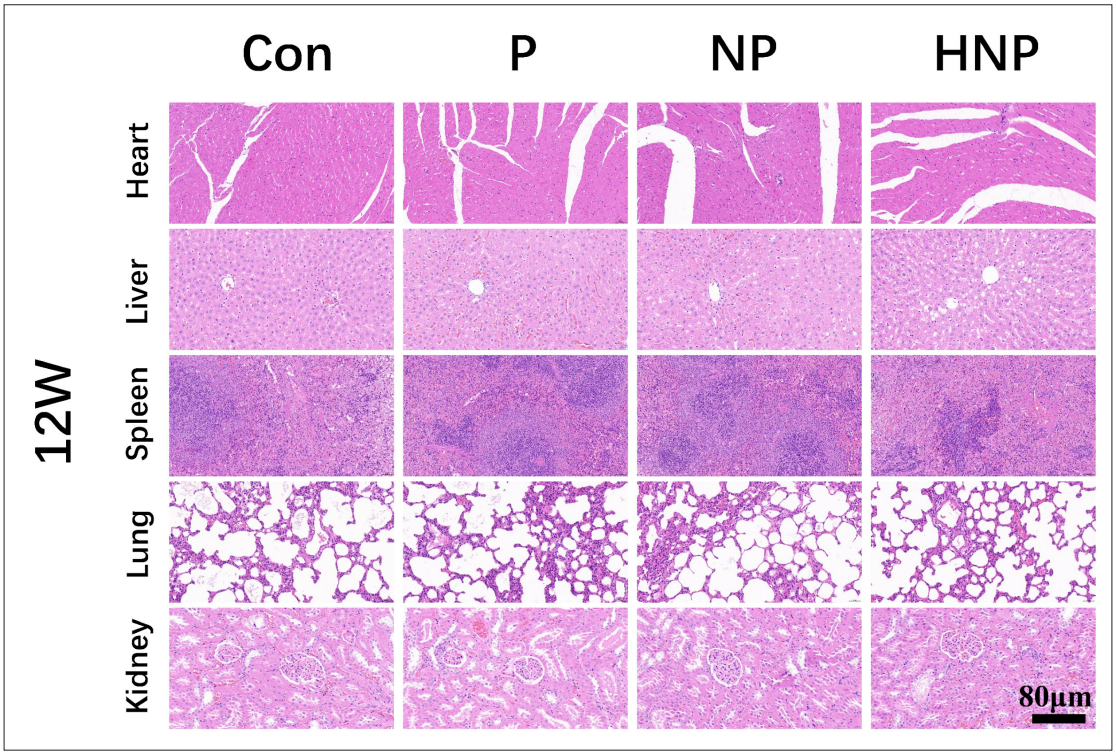

Figure 10. Hematoxylin and eosin staining of the heart, liver, spleen, lung, and kidney of rats at week 12 (12W) post-surgery. Magnification: 40×; scale bar: 80 μm. Abbreviations: Con: Control; HNP: Hydroxyapatite/montmorillonite nanoclay/polycaprolactone; NP: Nanoclay/polycaprolactone; P: Polycaprolactone.

formation at week 4 post-surgery. Although the amount of new bone increased at weeks 8 and 12, a substantial defect area remained, indicating the limited bone repair potential of the pure PCL scaffold. Compared with the P and NP groups, the HNP group exhibited significantly more new bone tissue at weeks 4 and 8 post-surgery. By week 12, the regenerated bone in the HNP group displayed more distinct trabecular and lamellar structures along the scaffold.

Quantitative analysis of BV/TV (%) (Figure 11B) and BMD (Figure 11C) at weeks 4, 8, and 12 post-surgery revealed that the HNP composite scaffold had the most significant effect on bone repair, whereas the blank control group had the poorest outcome. These differences were significant ($p < 0.01$). The order of bone repair effectiveness was: HNP > NP > P > Con.

3.3.3. Histological analysis

H&E staining and Masson's trichrome staining were performed to further confirm the osteoinductive effect of the HNP scaffold. The results were consistent with the micro-CT findings. As shown in Figures 12 and 13, at 4 weeks post-implantation, the HNP group exhibited more extensive mineralized bone formation in the rat calvarial defect area. In comparison, the NP group showed less new bone formation, whereas the Con and P groups demonstrated minimal to no new bone formation. At weeks 8 and 12 post-implantation, new bone tissue in all groups had further matured, with deep blue staining indicative of mature bone collagen. Notably, in the HNP group, mature bone tissue had formed and integrated into the scaffold structure, demonstrating the most pronounced osteogenic effect among all groups.

3.3.4. Immunohistochemical fluorescent staining

To further evaluate the immunomodulatory ability of the scaffolds *in vivo*, macrophage phenotypes were analyzed in calvarial specimens collected at weeks 4, 8, and 12 post-surgery. Double immunofluorescence staining for iNOS (red) and CD163 (green) was performed to assess macrophage polarization (Figure 14A). At week 4, the Con group showed a significantly higher density of proinflammatory M1 macrophage infiltration and markedly fewer anti-inflammatory M2 macrophages compared to the P, NP, and HNP groups. At weeks 8 and 12, extensive infiltration of M2 macrophages, known to promote bone tissue regeneration, was observed surrounding the HNP and NP scaffolds, with the HNP group exhibiting the most favorable results.

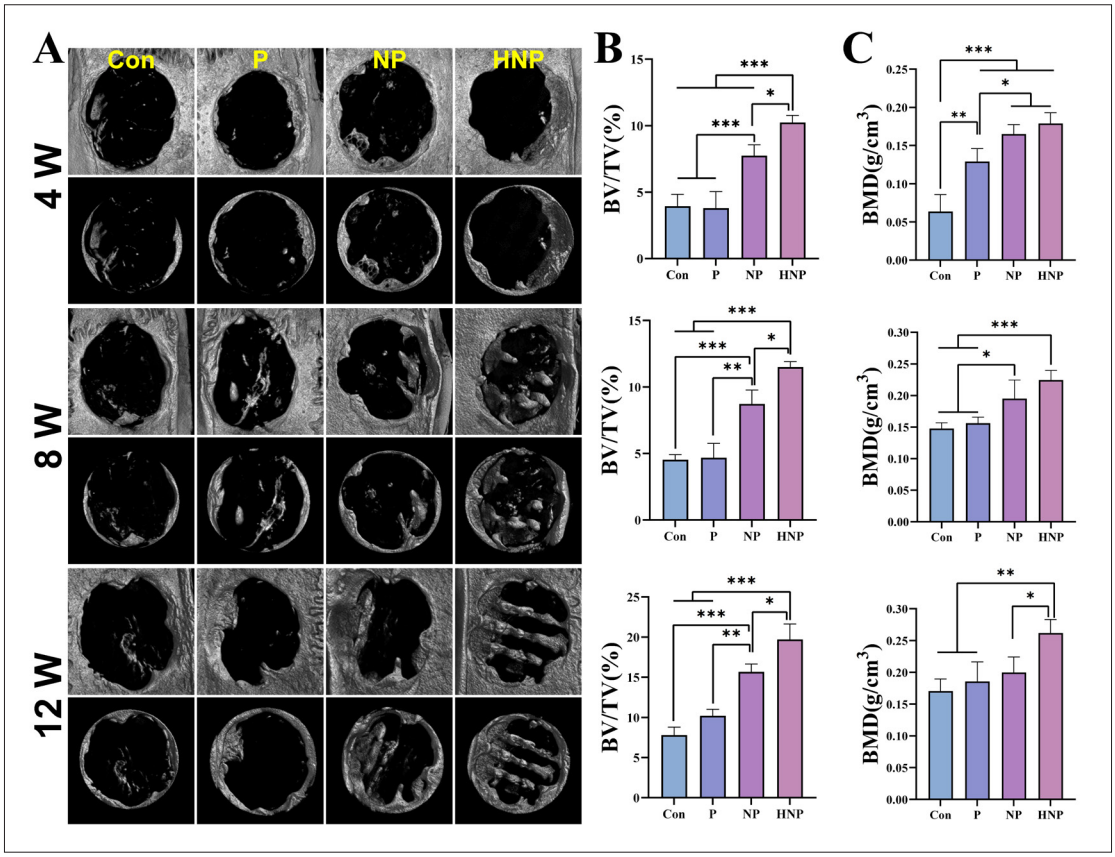

Figure 11. Micro-CT analysis of scaffolds in the rat calvarial defect model. (A) Micro-CT cross-sectional images of the rat calvarial defect site at 4, 8, and 12 weeks post-implantation. (B) Quantitative analysis of BV/TV (%) in the rat calvarial defect site at weeks 4, 8, and 12 post-implantation. (C) Quantitative analysis of BMD in the rat calvarial defect site at 4, 8, and 12 weeks post-implantation. Notes: $^{*}p < 0.05$, $^{**}p < 0.01$, $^{***}p < 0.001$. Abbreviations: BMD: Bone mineral density; BV/TV: Bone volume fraction; Con: Control; CT: Computed tomography; HNP: Hydroxyapatite/montmorillonite nanoclay/polycaprolactone; NP: Nanoclay/polycaprolactone; P: Polycaprolactone.

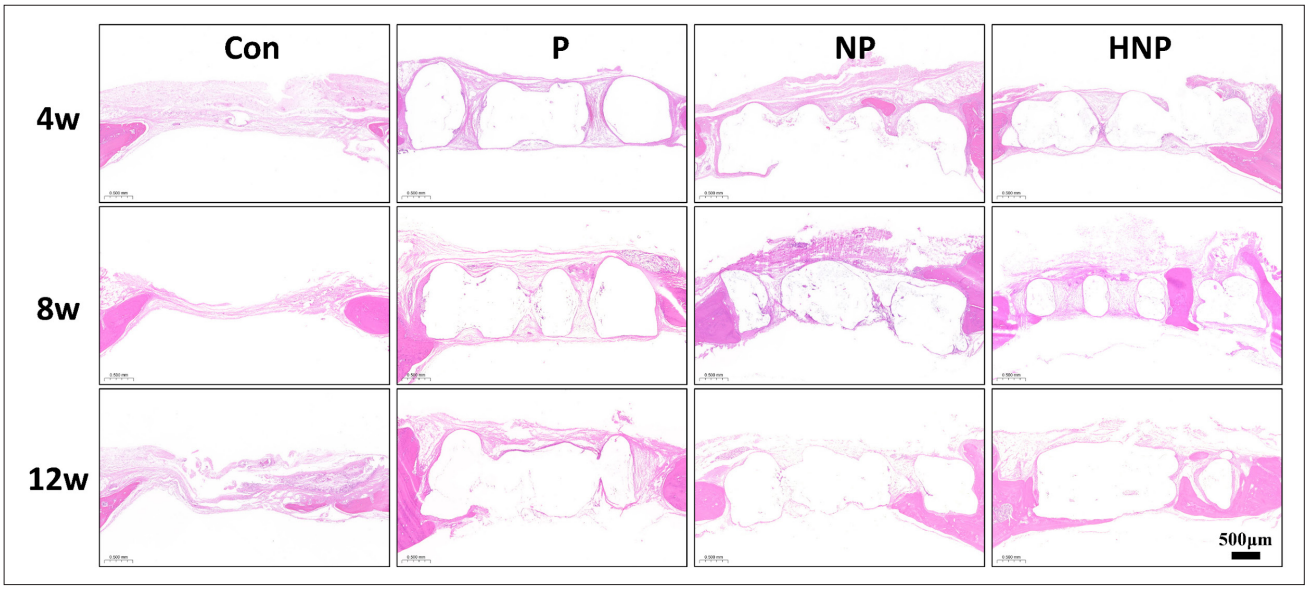

Figure 12. Hematoxylin and eosin staining of rat calvarial specimens at weeks 4, 8, and 12 postoperatively for each group. Magnification: 5×; scale bar: 500 μm. Abbreviations: Con: Control; HNP: Hydroxyapatite/montmorillonite nanoclay/polycaprolactone; NP: Nanoclay/polycaprolactone; P: Polycaprolactone.

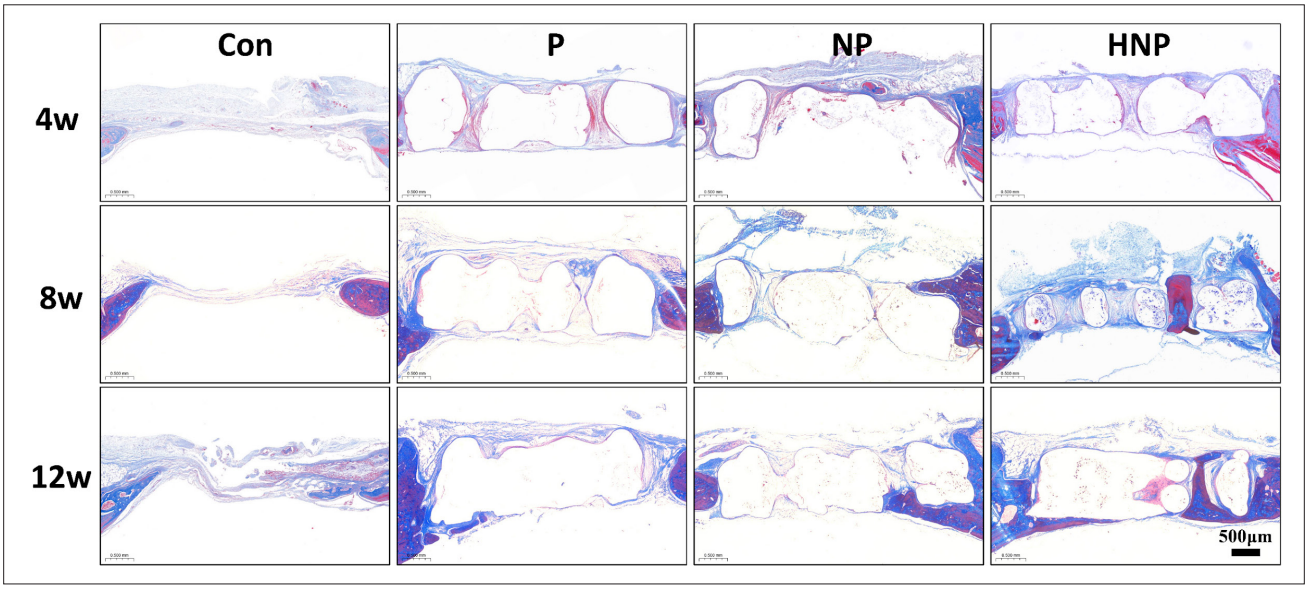

Figure 13. Masson's staining of rat calvarial specimens at weeks 4, 8, and 12 postoperatively for each group. Magnification: 5×; Scale bar: 500 μm. Abbreviations: Con: Control; HNP: Hydroxyapatite/montmorillonite nanoclay/polycaprolactone; NP: Nanoclay/polycaprolactone; P: Polycaprolactone.

Additionally, immunofluorescence staining for VEGF (red) and BMP-2 (green) was conducted to further assess the scaffolds' ability to promote osteogenesis and angiogenesis *in vivo* (Figure 14 B). At all time points (weeks 4, 8, and 12), VEGF and BMP-2 expression in the HNP group increased in a time-dependent manner, with significantly higher positive staining rates than those in the control group. These results suggest that the HNP scaffold has excellent immunomodulatory properties by promoting macrophage polarization toward the M2 phenotype, thus facilitating bone tissue regeneration. Furthermore, the HNP scaffold demonstrated strong angiogenic potential, enhancing nutrient supply to support the bone regeneration process.

4. Discussion

In this study, we investigated the potential of implanting 3D-printed HA/NC synergistically modified PCL composite scaffolds to promote bone regeneration through immunomodulation via macrophage polarization, both *in vitro* and *in vivo*. We successfully fabricated P, NP, and HNP scaffolds using 3D printing technology. Through *in vitro* experiments and an *in vivo* rat calvarial defect model, we confirmed that the incorporation of NC into the NP scaffold improved the immune micro-environment by inducing macrophage polarization from the proinflammatory M1 phenotype to the repair-oriented M2 phenotype, thereby promoting bone repair and angiogenesis. Moreover, the further incorporation of HA into the HNP scaffold enhanced both osteogenesis and angiogenesis, suggesting that the introduction of HA synergistically enhances the scaffold's repair efficacy.

Polycaprolactone, a semicrystalline polymer, has been widely used in tissue engineering because of its excellent biodegradability, biocompatibility, and mechanical properties.[39] However, the inherent hydrophobicity of pure PCL scaffolds significantly impairs cell adhesion, proliferation, and other biological behaviors, thereby limiting their application in bone repair.[40] To address these issues, numerous studies have demonstrated that modifying the surface of PCL or blending it with other polymers and inorganic materials can enhance its performance for specific applications.[41] Recently, NC has garnered attention in bone regeneration applications due to its unique layered structure. Its incorporation into polymers not only improves the mechanical strength of the material but also provides new strategies for functional scaffold design.[42,43] NC has been approved by the FDA for use in pharmaceutical products[44] and has been applied in various soft and hard tissue engineering contexts,[24] including skin,[45] bone,[46] and cartilage.[47] For example, chitosan hydrogel composites incorporating NC form interconnected microporous structures that significantly improve BMSC infiltration, proliferation, and osteogenic differentiation.[48] In this study, P, NP, and HNP scaffolds were successfully fabricated using 3D printing. SEM imaging and porosity testing of the scaffolds (Figure 3) revealed that the incorporation of NC increased the surface roughness and decreased the pore size of the NP scaffold, whereas the surface morphology of the

HNP scaffold was not significantly altered compared to the pure PCL scaffold. Furthermore, mechanical testing (Figure 4) showed that the HNP scaffold had significantly greater compressive strength than the P scaffold, though lower compressive strength than the NP scaffold. This result may be attributed to the random distribution of NC within the PCL matrix, where its layered structure maintains the integrity of the pore network, improving the mechanical properties while preserving stable porosity.[49] Additionally, the uniform dispersion of NC in the PCL matrix may create a "filling effect," reducing pore formation and enhancing mechanical performance.[50] The further inclusion of HA may have interfered with the interactions between PCL and NC, leading to the formation of pores on the surface of the HNP fibers. This may explain why the mechanical strength of the HNP scaffold was lower than that of the NP scaffold but still superior to that of the P scaffold. However, owing to the mechanical enhancement provided by NC, the HNP scaffold maintained good mechanical properties suitable for bone repair applications.

The interactions between polymer chains and the distinctive architecture of NC have been shown to generate interlayer voids and interparticle spaces, leading to alterations in the micro-structure that enhance osteoblast infiltration, proliferation, and differentiation.[46,50] These previous findings align with the results of the present study. Despite the lack of significant differences in porosity among the three scaffold groups, our experimental results revealed that, compared with both the P and NP scaffolds, the HNP scaffold notably enhanced cell adhesion and proliferation (Figure 5). This finding substantiates the notion that NC markedly improves the biocompatibility of PCL scaffolds. Additionally, the hydrophilicity of the scaffold plays a pivotal role in bone repair by optimizing the regenerative micro-environment, facilitating cell adhesion, enhancing tissue integration, and regulating drug release.[51–53] As illustrated in Figure 3B1 and 3B2, the incorporation of NC and HA effectively addressed the hydrophobic limitations of PCL, resulting in a significant increase in the hydrophilicity of the HNP scaffold. This, in turn, enhanced the scaffold's capacity to promote cell adhesion and proliferation. Notably, HA, a major inorganic component of human hard tissues, has emerged as a fundamental component in the development of bone repair materials, owing to its exceptional bioactivity and osteoconductivity.[54,55] Recent studies have demonstrated that NC and HA exhibit a pronounced synergistic effect upon incorporation into chitosan-gelatin composite scaffolds. The inclusion of HA not only reduces the scaffold's biodegradation rate but also increases its mineralization potential and mechanical properties, while the addition of NC further reinforces these characteristics.[35] Based on these mechanisms, the HNP scaffold in this study may promote osteogenesis through three primary pathways: first, the intrinsic bioactivity of HA directly stimulates cellular behavior; second, the synergistic interaction between NC and HA enhances the material's properties; and third, the porous structure formed on the scaffold fiber surface, along with the layered structure of NC, increases the specific surface area, thereby optimizing material exchange. Consequently, the HNP scaffold demonstrated significant advantages over both the P and NP groups in terms of cell adhesion, proliferation, and osteogenic differentiation.

Inflammation is a critical consideration following the implantation of engineered bone tissue scaffolds, with the initial inflammatory phase being more crucial than the subsequent active bone repair phase. Macrophages play pivotal roles in controlling the inflammatory response and maintaining bone homeostasis during bone regeneration.[56,57] The conversion of macrophage phenotypes and functions is a dynamic process, with M1 or M2 macrophages capable of interconverting under various stimuli.[58–60] The primary role of M1 macrophages is to promote the early inflammatory response to injury and facilitate the clearance of foreign materials or pathogens. However, after bone graft implantation, immune rejection may occur. In contrast, M2 macrophages play key anti-inflammatory roles and promote bone tissue repair.[61,62] Therefore, the efficient and timely transition from the M1 to the M2 phenotype is crucial for effective tissue healing. Although HA coatings have been shown to regulate macrophage polarization, the role of NC in modulating the immune micro-environment remains unclear. To explore whether the HNP scaffold can modulate the immune micro-environment and influence macrophage polarization to promote bone regeneration, we co-cultured P, NP, and HNP scaffolds with BMSCs and RAW264.7 cells *in vitro*. We then used qRT-PCR to detect the expression of osteogenesis-related genes (*Alp*, *Runx2*, and *Col1a1*) and macrophage-related genes for M1 (*Tnfa* and *Il1b*) and M2 (*Cd206* and *Arg*) phenotypes. Additionally, ELISA assays were used to quantify the levels of the pro-inflammatory cytokine IL-12 and the anti-inflammatory cytokine IL-10. The results confirmed our hypothesis that the HNP scaffold significantly upregulated the expression of osteogenesis-related genes compared with the NP group (Figure 6), indicating that the addition of HA further enhanced the osteogenic differentiation ability of the scaffold, consistent with the reported osteoinductive effects of HA.[34,63] Furthermore, compared with the NP scaffold, the HNP scaffold significantly downregulated M1 macrophage-related genes and upregulated M2 macrophage-related genes, while also reducing the levels of pro-inflammatory cytokine IL-12 and increasing the concentrations of anti-

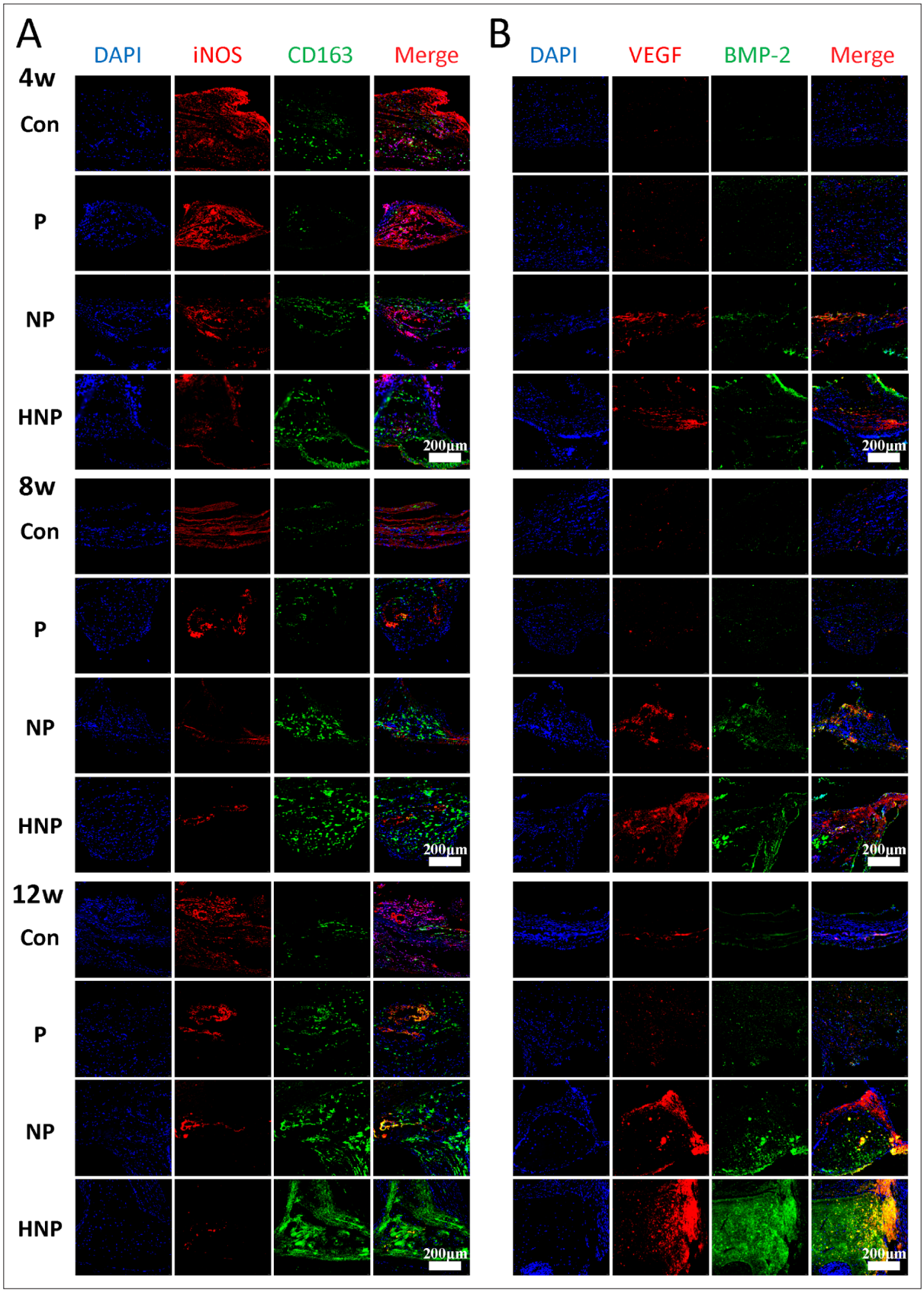
A
DAPI
iNOS
CD163
Merge
4w
Con
P
NP
HNP
8w
Con
P
NP
HNP
12w
Con
P
NP
HNP
200μm
B
DAPI
VEGF
BMP-2
Merge
200μm

Figure 14. Immunohistochemical fluorescence staining of the calvarial defect areas in Sprague– Dawley rats at weeks 4 (4w), 8 (8w), and 12 (12w) post-surgery. Scale bar: 200 μm; Magnification: 40×. (A) Immunofluorescence staining for iNOS (red) and CD163 (green) in the bone defect area at weeks 4, 8, and 12 post-surgery. (B) Immunofluorescence staining for VEGF and BMP-2 in the bone defect area at weeks 4, 8, and 12 post-surgery. Abbreviations: BMP-2: Bone morphogenetic protein 2; CD163: Cluster of differentiation 163; Con: Control; DAPI: 4',6-Diamidino-2-phenylindole; HNP: Hydroxyapatite/montmorillonite nanoclay/polycaprolactone; iNOS: Inducible nitric oxide synthase; NP: Nanoclay/polycaprolactone; P: Polycaprolactone; VEGF: Vascular endothelial growth factor.

inflammatory cytokine IL-10 (Figure 7). These findings suggest that both the NP and HNP scaffolds promote macrophage polarization toward the M2 phenotype to enhance bone regeneration, with the HNP scaffold showing superior effects.

To validate the *in vivo* bone repair effect of the scaffold, we established a rat calvarial defect model to assess the scaffold's biocompatibility and ability to promote bone repair. Peripheral blood parameters (Table 2) and H&E staining of major organs at weeks 4, 8, and 12 post-surgery (Figures 8–10) revealed that all groups of SD rats had normal peripheral blood values ($p > 0.05$), with no significant pathological lesions observed in the major organs, indicating good biocompatibility of our scaffolds. We also performed quantitative micro-CT analysis of the rat calvarial bones, including 3D reconstruction for qualitative assessment and quantitative analysis of BV/TV (%) and BMD (Figure 11). The results revealed that the HNP scaffoldsvvexhibited superior promotion of bone formation along the scaffold structure, occurring in the following order: HNP > NP > P > Con ($p > 0.05$). Histological staining confirmed these findings, showing that over time, new bone regeneration in the HNP group increased progressively and was significantly greater than in the other three groups (Figures 12 and 13).

In addition to immune modulation, angiogenesis is a key step in bone reconstruction during bone regeneration. Angiogenesis plays a vital role by enhancing the transport of oxygen, nutrients, and osteoprogenitor cells to the site of injury.[64] We employed double immunofluorescence staining to further investigate immunoregulation, osteogenic repair, and micro-vascular regeneration at the site of the calvarial defect in rats. As shown in Figure 14A, consistent with the *in vitro* qRT-PCR results, the HNP scaffold significantly promoted the polarization of macrophages from the M1 phenotype to the M2 phenotype in the rat calvarial defect area after implantation. Other than secreting various proinflammatory and anti-inflammatory cytokines, macrophages also release other factors that promote angiogenesis, tissue matrix remodeling, and local immune homeostasis during the later stages of bone healing, including VEGF and BMP-2.[65,66] As shown in Figure 14B, VEGF and BMP-2 expression in the HNP group increased in a time-dependent manner, with significantly higher positive staining rates than in the control group. These results confirm the immunomodulatory function of the HNP scaffold in bone regeneration. The HNP scaffold significantly promotes the polarization of macrophages from the proinflammatory M1 phenotype to the anti-inflammatory M2 phenotype in the calvarial defect area, effectively alleviating inflammation, promoting micro-vascular regeneration, and accelerating the repair of bone defects. The superior bone regeneration performance observed in the calvarial bones of rats implanted with the HNP scaffold may be attributed to two factors. First, the good dispersion of NC within the PCL matrix provides osteoblasts with better adhesion sites due to the high surface area and large aspect ratio of NC, whereas HA further induces osteoblastic responses, accelerating bone regeneration. Second, the synergistic effect of NC and HA promotes the polarization of macrophages from the M1 phenotype to the M2 phenotype, alleviating the local inflammatory micro-environment, promoting VEGF and BMP-2 secretion, and thereby inducing micro-vascular regeneration, which accelerates bone defect repair. HA/PCL composite scaffolds developed in previous studies have not yet achieved the ideal biological requirements for bone regeneration. While increasing the HA content in the scaffold can effectively enhance bone repair performance, a higher HA concentration significantly increases the brittleness of the scaffold material, making it less suitable for bone repair. In this study, although the mechanical strength of the HNP scaffold was lower than that of the NP scaffold, the HNP composite scaffold we developed exhibited significantly enhanced biological activity, including immunomodulatory and osteogenic activities, while retaining good mechanical strength, thus filling a critical gap in recent research.

This study explored the roles of macrophages in immune and inflammatory responses within the context of bone healing from the perspective of tissue engineering. However, the immune interactions between biomaterial scaffolds and the host are complex and involve not only macrophages but also potentially neutrophils, lymphocytes, and other inflammatory cells. Future studies may assess materials from the perspectives of neutrophils

and lymphocytes, potentially offering new insights and further understanding.

5. Conclusion

In this study, PCL composite scaffolds with either an NC modification alone or a synergistic HA/NC modification were successfully fabricated using 3D printing technology, with the aim of evaluating the potential of HA/NC in immune-regulated bone regeneration. Compared with the pure PCL and NP scaffolds, the HNP scaffold significantly improved cell adhesion, proliferation, osteogenic differentiation, and macrophage polarization toward the M2 phenotype, while maintaining favorable mechanical properties. These effects promoted the secretion of osteogenesis-related cytokines and the regeneration of micro-vascular structures, thereby establishing an immune micro-environment conducive to bone regeneration and markedly accelerating the repair of calvarial defects in SD rats. In conclusion, our findings suggest that the 3D-printed HNP composite scaffold can induce M2 macrophage polarization to enhance bone tissue repair and angiogenesis, highlighting its promising potential as a candidate for bone tissue engineering.

Acknowledgments

None.

Funding

This research was supported by the National Natural Science Foundation of China (82160577, 32000964), the Key Program for Science and Technology Project of Guizhou Province (ZK [2021] 007), the Zunyi City Innovation Team Fund (Zunyi Science Talent (2024) No. 4), Guangdong Province Science and Technology Plan Project (2024A1515012265), the Hainan Academician Innovation Center (Nanfan Medical Materials and Health Technology Innovation Center) (2022GDASZH-2022020402-01).

Conflict of interest

We declare that we have no financial and personal relationships with other people or organizations that can inappropriately influence our work, there is no professional or other personal interest of any nature or kind in any product, service and/or company that could be construed as influencing the position presented in, or the review of, the manuscript entitled.

Author contributions

Conceptualization: Xiang Li, Weikang Xu and Qingde Wa
Formal analysis: Xiang Li, Zhenyu Wen, Jiaxiang Song, Hao Tang, Wanshun Liu, Xitao Linghu
Investigation: Xiang Li, Zhenyu Wen
Methodology: Xiang Li, Zhenyu Wen
Supervision: Weikang Xu and Qingde Wa
Writing–original draft: Xiang Li, Zhenyu Wen
Writing–review & editing: Shuai Huang, Weikang Xu, Qingde Wa

Ethics approval and consent to participate

All animal experiments were performed under the protocol approved by the Institutional Animal Care and Use Committee of Guangdong Quality Supervision and Testing Station for Medical and Health Care Appliances.

Consent for publication

Not applicable.

Availability of data

Data from this study are available from the corresponding author upon reasonable request.

References

1. Wubneh A, Tsekoura EK, Ayranci C, Uludağ H. Current state of fabrication technologies and materials for bone tissue engineering. *Acta Biomater*. 2018;80:1-30. doi: 10.1016/j.actbio.2018.09.031
2. Zhang X, Yang Y, Yang Z, *et al*. Four-dimensional printing and shape memory materials in bone tissue engineering. *Int J Mol Sci*. 2023;24(1):814. doi: 10.3390/ijms24010814
3. Wang W, Yeung KWK. Bone grafts and biomaterials substitutes for bone defect repair: a review. *Bioact Mater*. 2017;2(4):224-247. doi: 10.1016/j.bioactmat.2017.05.007
4. Schmidt AH. Autologous bone graft: is it still the gold standard? *Injury*. 2021;52(Suppl 2):S18-S22. doi: 10.1016/j.injury.2021.01.043
5. Feng Y, Zhu S, Mei D, *et al*. Application of 3D printing technology in bone tissue engineering: a review. *Curr Drug Deliv*. 2021;18(7):847-861. doi: 10.2174/1567201817999201113100322
6. Sadowska JM, Ginebra M-P. Inflammation and biomaterials: role of the immune response in bone regeneration by inorganic scaffolds. *J Mater Chem B*. 2020;8(41):9404-9427. doi: 10.1039/d0tb01379j
7. He J, Chen G, Liu M, *et al*. Scaffold strategies for modulating immune microenvironment during bone regeneration. *Mater Sci Eng C Mater Biol Appl*. 2020;108:110411. doi: 10.1016/j.msec.2019.110411

8. Zheng Z-W, Chen Y-H, Wu D-Y, *et al*. Development of an accurate and proactive immunomodulatory strategy to improve bone substitute material-mediated osteogenesis and angiogenesis. *Theranostics*. 2018;8(19):5482-5500. doi: 10.7150/thno.28315

9. Dutta SD, Ganguly K, Patil TV, Randhawa A, Lim KT. Unraveling the potential of 3D bioprinted immunomodulatory materials for regulating macrophage polarization: State-of-the-art in bone and associated tissue regeneration. *Bioact Mater*. 2023;28:284-310. doi: 10.1016/j.bioactmat.2023.05.014

10. Yang N, Liu Y. The role of the immune microenvironment in bone regeneration. *Int J Med Sci*. 2021;18(16):3697-3707. doi: 10.7150/ijms.61080

11. Lee J, Byun H, Madhurakkat Perikamana SK, Lee S, Shin H. Current advances in immunomodulatory biomaterials for bone regeneration. *Adv Healthc Mater*. 2019;8(4):e1801106. doi: 10.1002/adhm.201801106

12. Xie Y, Hu C, Feng Y, *et al*. Osteoimmunomodulatory effects of biomaterial modification strategies on macrophage polarization and bone regeneration. *Regen Biomater*. 2020;7(3):233-245. doi: 10.1093/rb/rbaa006

13. Locati M, Curtale G, Mantovani A. Diversity, mechanisms, and significance of macrophage plasticity. *Annu Rev Pathol*. 2020;15:123-147. doi: 10.1146/annurev-pathmechdis-012418-012718

14. Tian Y, Li Y, Liu J, *et al*. Photothermal therapy with regulated Nrf2/NF-κB signaling pathway for treating bacteria-induced periodontitis. *Bioact Mater*. 2022;9:428-445. doi: 10.1016/j.bioactmat.2021.07.033

15. Zheng K, Niu W, Lei B, Boccaccini AR. Immunomodulatory bioactive glasses for tissue regeneration. *Acta Biomater*. 2021;133:168-186. doi: 10.1016/j.actbio.2021.08.023

16. Lin Z, Shen D, Zhou W, *et al*. Regulation of extracellular bioactive cations in bone tissue microenvironment induces favorable osteoimmune conditions to accelerate in situ bone regeneration. *Bioact Mater*. 2021;6(8):2315-2330. doi: 10.1016/j.bioactmat.2021.01.018

17. Liu X, Chen M, Luo J, *et al*. Immunopolarization-regulated 3D printed-electrospun fibrous scaffolds for bone regeneration. *Biomaterials*. 2021;276:121037. doi: 10.1016/j.biomaterials.2021.121037

18. Jin S, Yang R, Chu C, *et al*. Topological structure of electrospun membrane regulates immune response, angiogenesis and bone regeneration. *Acta Biomater*. 2021;129:148-158. doi: 10.1016/j.actbio.2021.05.042

19. Arif ZU, Khalid MY, Noroozi R, Sadeghianmaryan A, Jalalvand M, Hossain M. Recent advances in 3D-printed polylactide and polycaprolactone-based biomaterials for tissue engineering applications. *Int J Biol Macromol*. 2022;218:930-968. doi: 10.1016/j.ijbiomac.2022.07.140

20. Gómez-Lizárraga KK, Flores-Morales C, Del Prado-Audelo ML, Álvarez-Pérez MA, Piña-Barba MC, Escobedo C. Polycaprolactone- and polycaprolactone/ceramic-based 3D-bioplotted porous scaffolds for bone regeneration: a comparative study. *Mater Sci Eng C*. 2017;79:326-335. doi: 10.1016/j.msec.2017.05.003

21. Nobles KP, Janorkar AV, Williamson RS. Surface modifications to enhance osseointegration–resulting material properties and biological responses. *J Biomed Mater Res B Appl Biomater*. 2021;109(11):1909-1923. doi: 10.1002/jbm.b.34835

22. Druzian DM, Bonazza GKC, Sangoi GG, *et al*. Fabrication and properties of the montmorillonite/nanobioglass hybrid reinforcement from agroindustrial waste for bone regeneration. *ACS Appl Mater Interfaces*. 2024;16(15):19391-19410. doi: 10.1021/acsami.4c02160

23. Gaharwar AK, Cross LM, Peak CW, *et al*. 2D nanoclay for biomedical applications: regenerative medicine, therapeutic delivery, and additive manufacturing. *Adv Mater*. 2019;31(23):e1900332. doi: 10.1002/adma.201900332

24. Katti KS, Jasuja H, Jaswandkar SV, Mohanty S, Katti DR. Nanoclays in medicine: a new frontier of an ancient medical practice. *Mater Adv*. 2022;3(20):7484-7500. doi: 10.1039/d2ma00528j

25. Bee S-L, Abdullah MAA, Bee S-T, Sin LT, Rahmat AR. Polymer nanocomposites based on silylated-montmorillonite: a review. *Prog Polym Sci*. 2018;85:57-82. doi: 10.1016/j.progpolymsci.2018.07.003

26. Li Y, Yang G, Wang Y, *et al*. Osteoimmunity-regulating nanosilicate-reinforced hydrogels for enhancing osseointegration. *J Mater Chem B*. 2023;11(41):9933-9949. doi: 10.1039/d3tb01509b

27. Stodolak-Zych E, Kurpanik R, Dzierzkowska E, *et al*. Effects of montmorillonite and gentamicin addition on the properties of electrospun polycaprolactone fibers. *Materials (Basel)*. 2021;14(22):6905. doi: 10.3390/ma14226905

28. Sadeghianmaryan A, Yazdanpanah Z, Soltani YA, Sardroud HA, Nasirtabrizi MH, Chen X. Curcumin-loaded electrospun polycaprolactone/montmorillonite nanocomposite: wound dressing application with anti-bacterial and low cell toxicity properties. *J Biomater Sci Polym Ed*. 2020;31(2):169-187. doi: 10.1080/09205063.2019.1680928

29. Szcześ A, Hołysz L, Chibowski E. Synthesis of hydroxyapatite for biomedical applications. *Adv Colloid Interface Sci*. 2017;249:321-330. doi: 10.1016/j.cis.2017.04.007

30. Ribeiro N, Sousa A, Cunha-Reis C, *et al*. New prospects in skin regeneration and repair using nanophased hydroxyapatite embedded in collagen nanofibers. *Nanomedicine*. 2021;33:102353.
doi: 10.1016/j.nano.2020.102353

31. Helaehil JV, Lourenço CB, Huang B, *et al*. In vivo investigation of polymer-ceramic PCL/HA and PCL/β-TCP 3D composite scaffolds and electrical stimulation for bone regeneration. *Polymers (Basel)*. 2021;14(1):65.
doi: 10.3390/polym14010065

32. Rezania N, Asadi-Eydivand M, Abolfathi N, Bonakdar S, Mehrjoo M, Solati-Hashjin M. Three-dimensional printing of polycaprolactone/hydroxyapatite bone tissue engineering scaffolds mechanical properties and biological behavior. *J Mater Sci Mater Med*. 2022;33(3):31.
doi: 10.1007/s10856-022-06653-8

33. Petretta M, Gambardella A, Desando G, *et al*. Multifunctional 3D-printed magnetic polycaprolactone/hydroxyapatite scaffolds for bone tissue engineering. *Polymers (Basel)*. 2021;13(21):3825.
doi: 10.3390/polym13213825

34. Shang L, Shao J, Ge S. Immunomodulatory properties: the accelerant of hydroxyapatite-based materials for bone regeneration. *Tissue Eng Part C Methods*. 2022;28(8):377-392.
doi: 10.1089/ten.TEC.2022.00111112

35. Katti DR, Sharma A, Ambre AH, Katti KS. Molecular interactions in biomineralized hydroxyapatite amino acid modified nanoclay: in silico design of bone biomaterials. *Mater Sci Eng C Mater Biol Appl*. 2015;46:207-217.
doi: 10.1016/j.msec.2014.07.057

36. Bhowmick A, Banerjee SL, Pramanik N, *et al*. Organically modified clay supported chitosan/hydroxyapatite-zinc oxide nanocomposites with enhanced mechanical and biological properties for the application in bone tissue engineering. *Int J Biol Macromol*. 2018;106:11-19.
doi: 10.1016/j.ijbiomac.2017.07.168

37. Bhowmick A, Jana P, Pramanik N, *et al*. Multifunctional zirconium oxide doped chitosan based hybrid nanocomposites as bone tissue engineering materials. *Carbohydr Polym*. 2016;151:879-888.
doi: 10.1016/j.carbpol.2016.06.034

38. Cho SJ, Jung SM, Kang M, Shin HS, Youk JH. Preparation of hydrophilic PCL nanofiber scaffolds via electrospinning of PCL/PVP-b-PCL block copolymers for enhanced cell biocompatibility. *Polymer*. 2015/07/09/ 2015;69:95-102.
doi: 10.1016/j.polymer.2015.05.037

39. Neufurth M, Wang X, Wang S, *et al*. 3D printing of hybrid biomaterials for bone tissue engineering: calcium-polyphosphate microparticles encapsulated by polycaprolactone. *Acta Biomater*. 2017;64:377-388.
doi: 10.1016/j.actbio.2017.09.031

40. Liang H-Y, Lee W-K, Hsu J-T, *et al*. Polycaprolactone in bone tissue engineering: a comprehensive review of innovations in scaffold fabrication and surface modifications. *J Funct Biomater*. 2024;15(9):243.
doi: 10.3390/jfb15090243

41. Esmaeili J, Jalise SZ, Pisani S, *et al*. Development and characterization of Polycaprolactone/chitosan-based scaffolds for tissue engineering of various organs: a review. *Int J Biol Macromol*. 2024;272(Pt 2):132941.
doi: 10.1016/j.ijbiomac.2024.132941

42. Mousa M, Evans ND, Oreffo ROC, Dawson JI. Clay nanoparticles for regenerative medicine and biomaterial design: a review of clay bioactivity. *Biomaterials*. 2018;159:204-214.
doi: 10.1016/j.biomaterials.2017.12.024

43. Jansson M, Lenton S, Plivelic TS, Skepö M. Intercalation of cationic peptides within Laponite layered clay minerals in aqueous suspensions: the effect of stoichiometry and charge distance matching. *J Colloid Interface Sci*. 2019;557:767-776.
doi: 10.1016/j.jcis.2019.09.055

44. Baveloni FG, Riccio BVF, Di Filippo LD, Fernandes MA, Meneguin AB, Chorilli M. Nanotechnology-based drug delivery systems as potential for skin application: a review. *Curr Med Chem*. 2021;28(16):3216-3248.
doi: 10.2174/0929867327666200831125656

45. Sajjad W, Khan T, Ul-Islam M, *et al*. Development of modified montmorillonite-bacterial cellulose nanocomposites as a novel substitute for burn skin and tissue regeneration. *Carbohydr Polym*. 2019;206:548-556.
doi: 10.1016/j.carbpol.2018.11.023

46. Cui Z-K, Kim S, Baljon JJ, Wu BM, Aghaloo T, Lee M. Microporous methacrylated glycol chitosan-montmorillonite nanocomposite hydrogel for bone tissue engineering. *Nat Commun*. 2019;10(1):3523.
doi: 10.1038/s41467-019-11511-3

47. Sheng R, Chen J, Wang H, *et al*. Nanosilicate-reinforced silk fibroin hydrogel for endogenous regeneration of both cartilage and subchondral bone. *Adv Healthc Mater*. 2022;11(17):e2200602.
doi: 10.1002/adhm.202200602

48. Nitya G, Nair GT, Mony U, Chennazhi KP, Nair SV. In vitro evaluation of electrospun PCL/nanoclay composite scaffold for bone tissue engineering. *J Mater Sci Mater Med*. 2012;23(7):1749-1761.
doi: 10.1007/s10856-012-4647-x

49. Sukhanova A, Boyandin A, Ertiletskaya N, *et al*. Composite polymer granules based on poly-ε-caprolactone and montmorillonite prepared by solution-casting and melt extrusion. *Polymers (Basel)*. 2023;15(20):4099.
doi: 10.3390/polym15204099

50. Zhu B, Bai T, Wang P, Wang Y, Liu C, Shen C. Selective dispersion of carbon nanotubes and nanoclay in biodegradable poly(ε-caprolactone)/poly(lactic acid) blends with improved toughness, strength and thermal stability. *Int J Biol Macromol*. 2020;153:1272-1280.

doi: 10.1016/j.ijbiomac.2019.10.262

51. Dhania S, Rani R, Kumar R, Thakur R. Fabricated polyhydroxyalkanoates blend scaffolds enhance cell viability and cell proliferation. *J Biotechnol*. 2023;361:30-40. doi: 10.1016/j.jbiotec.2022.11.014

52. Boyan BD, Lotz EM, Schwartz Z. Roughness and hydrophilicity as osteogenic biomimetic surface properties. *Tissue Eng Part A*. 2017;23(23-24):1479-1489. doi: 10.1089/ten.TEA.2017.0048

53. Ijaola AO, Akamo DO, Damiri F, *et al*. Polymeric biomaterials for wound healing applications: a comprehensive review. *J Biomater Sci Polym Ed*. 2022;33(15):1998-2050. doi: 10.1080/09205063.2022.2088528

54. Yang H, Gao H, Wang Y. Hollow hydroxyapatite microsphere: a promising carrier for bone tissue engineering. *J Microencapsul*. 2016;33(5):421-426. doi: 10.1080/02652048.2016.1202347

55. Huang H, Yang A, Li J, *et al*. Preparation of multigradient hydroxyapatite scaffolds and evaluation of their osteoinduction properties. *Regen Biomater*. 2022; 9:rbac001. doi: 10.1093/rb/rbac001

56. Yan L, Wang J, Cai X, *et al*. Macrophage plasticity: signaling pathways, tissue repair, and regeneration. *MedComm (2020)*. 2024;5(8):e658. doi: 10.1002/mco2.658

57. Takayanagi H. Osteoimmunology: shared mechanisms and crosstalk between the immune and bone systems. *Nat Rev Immunol*. 2007;7(4):292-304. doi: 10.1038/nri2062.

58. Li C, Xu MM, Wang K, Adler AJ, Vella AT, Zhou B. Macrophage polarization and meta-inflammation. *Transl Res*. 2018;191:29-44. doi: 10.1016/j.trsl.2017.10.004

59. Shapouri-Moghaddam A, Mohammadian S, Vazini H, *et al*. Macrophage plasticity, polarization, and function in health and disease. *J Cell Physiol*. 2018;233(9): 6425-6440. doi: 10.1002/jcp.26429

60. Wynn TA, Vannella KM. Macrophages in tissue repair, regeneration, and fibrosis. *Immunity*. 2016;44(3):450-462. doi: 10.1016/j.immuni.2016.02.015

61. Rőszer T. Understanding the mysterious M2 macrophage through activation markers and effector mechanisms. *Mediators Inflamm*. 2015;2015:816460. doi: 10.1155/2015/816460

62. Wynn TA, Chawla A, Pollard JW. Macrophage biology in development, homeostasis and disease. *Nature*. 2013;496(7446):445-455. doi: 10.1038/nature12034

63. Mahon OR, Browe DC, Gonzalez-Fernandez T, *et al*. Nano-particle mediated M2 macrophage polarization enhances bone formation and MSC osteogenesis in an IL-10 dependent manner. *Biomaterials*. 2020;239:119833. doi: 10.1016/j.biomaterials.2020.119833

64. Lee E-J, Jain M, Alimperti S. Bone microvasculature: stimulus for tissue function and regeneration. *Tissue Eng Part B Rev*. 2021;27(4):313-329. doi: 10.1089/ten.TEB.2020.0154

65. Yu Y, Dai K, Gao Z, *et al*. Sulfated polysaccharide directs therapeutic angiogenesis via endogenous VEGF secretion of macrophages. *Sci Adv*. 2021;7(7):eabd8217. doi: 10.1126/sciadv.abd8217

66. Poon B, Kha T, Tran S, Dass CR. Bone morphogenetic protein-2 and bone therapy: successes and pitfalls. *J Pharm Pharmacol*. 2016;68(2):139-147. doi: 10.1111/jphp.12506